Range-dynamical low-rank split-step Fourier method for the parabolic wave equation

Aaron Charous[a] (iD) and Pierre F. J. Lermusiaux[b] (iD)

Department of Mechanical Engineering, Center for Computational Science and Engineering, Massachusetts Institute of Technology, Cambridge, Massachusetts 02139, USA

ABSTRACT:

Numerical solutions to the parabolic wave equation are plagued by the curse of dimensionality coupled with the Nyquist criterion. As a remedy, a new range-dynamical low-rank split-step Fourier method is developed. The integration scheme scales sub-linearly with the number of classical degrees of freedom in the transverse directions. It is orders of magnitude faster than the classic full-rank split-step Fourier algorithm and saves copious amounts of storage space. This enables numerical solutions of the parabolic wave equation at higher frequencies and on larger domains, and simulations may be performed on laptops rather than high-performance computing clusters. Using a rank-adaptive scheme to optimize the low-rank equations further ensures the approximate solution is highly accurate and efficient. The methodology and algorithms are demonstrated on realistic high-resolution data-assimilative ocean fields in Massachusetts Bay for two three-dimensional acoustic configurations with different source locations and frequencies. The acoustic pressure, transmission loss, and phase solutions are analyzed in the two geometries with seamounts and canyons across and along Stellwagen Bank. The convergence with the rank of the subspace and the properties of the rank-adaptive scheme are demonstrated, and all results are successfully compared with those of the full-rank method when feasible. © *2024 Acoustical Society of America*. https://doi.org/10.1121/10.0032470

I. INTRODUCTION

Wave propagation is pertinent to many scientific and engineering disciplines such as oceanography, seismology, acoustics, and optics. For propagation in complex media, both forward problems—where one predicts how a wave propagates in a known environment—and inverse problems—where one attempts to determine model/environmental parameters given observational data about wave propagation in the said environment—require numerical methods to provide accurate solutions. In this paper, we restrict our attention to the acoustic wave equation for propagation in the three spatial dimensions,

$$\rho \nabla \cdot \left(\frac{1}{\rho} \nabla p \right) - \frac{1}{c^2} \frac{\partial^2 p}{\partial t^2} = f, \tag{1}$$

where p is the acoustic pressure field, ρ the density field of the media, c is the sound speed field of the media, t time, and f some forcing field. Our specific domain of interest is underwater acoustics.

Unfortunately, numerically solving this hyperbolic partial differential equation (PDE) is often too computationally expensive in three dimensions and/or at mid-to-high frequencies. The Nyquist criterion requires we sample spatially at least twice per wavelength as well as temporally at least

twice per period. This would be a minimal resolution in space-time but, nonetheless, a fine mesh for many problems, making the direct numerical simulation of the acoustic wave Eq. (1) in complex environments such as the ocean intractable. Several approximations can be made, such as ray methods (Cervenỳ, 2001; Lichte, 1919), wavenumber integration (DiNapoli and Deavenport, 1980; Ewing *et al.*, 1957; Jardetzky, 1953; Kutschale, 1973), normal-mode methods (Ide *et al.*, 1947; Pekeris, 1948; Williams, 1970), and parabolic wave equations (Hardin, 1973; Leontovich and Fock, 1946), all of which are discussed in Jensen *et al.* (2011). Frequently used three-dimensional (3D) parabolic acoustic propagation codes include RAM (Collins *et al.*, 1996), PEREGRINE (Heaney and Campbell, 2016), and FOR3D (Botseas *et al.*, 1987). Solutions to the 3D parabolic equation (PE) in complex ocean environments have been studied by Duda (2006), Heaney and Campbell (2016), Lin (2019), and Oliveira *et al.* (2021), and efforts to accelerate computation via parallelization have been investigated by Castor and Sturm (2008), Collins (1993), and Xu and Tang (2019). Nevertheless, numerically solving large 3D PE problems accurately remains expensive or infeasible, and the goal of this paper is to enable such high-resolution solutions by developing new optimal range-dynamical low-rank schemes.

Our emphasis is on the narrow-angle, density-reduced parabolic wave equation, obtained as follows. First, Fourier-transforming Eq. (1) in time gives the Helmholtz equation,

[a] Email: acharous@mit.edu
[b] Email: pierrel@mit.edu

$$\rho\nabla\cdot\left(\frac{1}{\rho}\nabla P\right)+k^2P=F, \qquad (2)$$

where P and F are the time-Fourier-transformed acoustic pressure and forcing functions, respectively, $k=\omega/c$ is the wavenumber, and ω is the frequency (in radians per second). The Helmholtz equation is elliptic, meaning the whole spatial domain must be solved for simultaneously. A further approximation is then made by assuming the acoustic medium is relatively smooth and weakly range-dependent, which allows converting the elliptic PDE into a parabolic one. In doing so, the numerical PDE solution is marched forward along a chosen principal axis or range, which is here denoted as x (Collins and Siegmann, 2019). The derivation is provided in Collins and Siegmann (2019) and Jensen *et al.* (2011). The final narrow-angle PE is given by

$$\frac{\partial\psi}{\partial x}=\left[\frac{ik_0}{2}(\tilde{n}^2-1)+\frac{i}{2k_0}\nabla_\perp^2\right]\psi, \qquad (3)$$

where ψ is a density-reduced wave envelope related to the acoustic pressure Fourier-transformed in time by $P=\sqrt{\rho}e^{ik_0x}\psi$, k_0 is a reference wavenumber defined by $k_0=\omega/c_0$, where c_0 is the reference sound speed, $\nabla_\perp^2$ is the Laplacian in the transverse directions, y and z, and $\tilde{n}$ is the complex effective refractive index given by

$$\tilde{n}^2=\frac{c_0^2}{c^2}\left[1+i\frac{\alpha^{(\lambda)}}{20\pi\log_{10}(e)}\right]$$
$$+\frac{1}{2k_0^2}\left[\frac{1}{\rho}\nabla^2\rho-\frac{3}{2\rho^2}\nabla\rho\cdot\nabla\rho\right], \qquad (4)$$

where $\alpha^{(\lambda)}$ is the attenuation coefficient in decibels per wavelength, dB/λ. This complex refractive index allows us to incorporate attenuation and density variations.

Despite these approximations, 3D numerical solutions to the narrow-angle parabolic wave equation [Eq. (3)] are still computationally expensive (Lee *et al.*, 1995; Lin *et al.*, 2019). This is primarily due to the spatial Nyquist criterion, resulting in an extremely dense mesh. In a typical ocean acoustic application, there can be millions of degrees of freedom in each range slice. At higher frequencies, one may approach billions of degrees of freedom. Not only does this make computing solutions slow, but it also makes them difficult to store. In contrast to the approximations made earlier where the PDE itself was modified, we propose an alternative approximation. We decompose the solution using a range-dynamical separation of variables in the transverse directions and apply a dynamically orthogonal (DO) low-rank approximation, thus drastically reducing the dimensionality of the problem while still abiding by the Nyquist criterion and high resolution. Building off the split-step Fourier (SSF) algorithm (Hardin, 1973), we incorporate projection operators approximated by rank-adaptive retractions. The retractions also project the updated solution onto a low-rank manifold and prevent the dimensionality of the

reduced-order solution from growing exponentially with range. By asymptotically approximating the aforementioned projection operator, the retractions significantly reduce computational cost while dynamically adjusting the rank with range, enhancing both accuracy and efficiency. We demonstrate the efficacy of the new method by evaluating it on realistic high-resolution data-assimilative ocean fields with internal tides, eddies, and jets around Stellwagen Bank in Massachusetts Bay. We highlight acoustic configurations with different source locations and frequencies and two geometries with seamounts and canyons, across and along the Bank. We study convergence with the rank of the subspace, illustrate the rank-adaptive scheme, and compare results with those of the full-rank method when feasible.

In what follows, Sec. II describes the new methodology for solving the parabolic wave equation. The classic SSF algorithm is briefly reviewed before our novel range-dynamical low-rank split-step Fourier (lr-SSF) method is obtained. Section III discusses the algorithms and implementation of the new operators required for the lr-SSF method and analyzes the computational advantages over the classic full-rank SSF. In addition, we detail a rank-adaptive algorithm that adjusts the rank of the solution for optimal solution fidelity and computational efficiency. In Sec. IV, we demonstrate the new method in Massachusetts Bay with simulations at 75 and 750 Hz and analyze its properties and performance. Compared to the classic SSF, the range-dynamical lr-SSF significantly reduces computational costs without loss of accuracy, which is a key result we emphasize. Section V provides some closing remarks and future research directions.

II. METHODOLOGY

A. SSF

The SSF algorithm (Hardin, 1973) for solving the narrow-angle parabolic wave equation [Eq. (3)] is well known. The key to the algorithm is splitting the right-hand side of Eq. (3) into two components, a reaction operator A and a diffusion operator B:

$$A\equiv\frac{ik_0}{2}(\tilde{n}^2-1), \quad B\equiv\frac{i}{2k_0}\left(\frac{\partial^2}{\partial y^2}+\frac{\partial^2}{\partial z^2}\right).$$

Now, instead of integrating Eq. (3) directly, we may integrate A and B separately. A second-order accurate integration algorithm known as Strang splitting (Strang, 1968) is as follows:

(1) Integrate $\partial\psi/\partial x=A\psi$ for $x\in[x_0,x_0+\Delta x/2]$ with initial conditions $\psi(x_0,y,z)$.
(2) Integrate $\partial\psi/\partial x=B\psi$ for $x\in[x_0,x_0+\Delta x]$ with initial conditions from step 1.
(3) Integrate $\partial\psi/\partial x=A\psi$ for $x\in[x_0+\Delta x/2,x_0+\Delta x]$ with initial conditions from step 2.

Reviews of splitting methods are provided in McLachlan and Quispel (2002) and Jensen *et al.* (2011, Sec. 6.5). Splitting the PDE into different components is useful for two reasons. First, the split PDEs may be integrated exactly in closed form. Second, after discretizing the PDE,

Aaron Charous and Pierre F. J. Lermusiaux

the reaction operator is diagonal when applied in the spatial domain, and the diffusion term is diagonal and spectrally accurate when applied in the frequency/Fourier domain. By separating A and B appropriately, each of the operators may be applied in their respective domains.

The y-z discretized approximations to ψ and $\tilde{n}$ are denoted as $\boldsymbol{\Psi}$ and $\hat{n}$, respectively (see Table I). Unrolling steps 1–3, one obtains a second-order SSF Fourier integrator,

$$
\begin{aligned}
\boldsymbol{\Psi}(x+\Delta x) = \exp&\left(\frac{ik_0}{2}\int_{x+\Delta x/2}^{x+\Delta x}(\hat{n}^2(s)-1)ds\right)\\
&\cdot\mathcal{F}^{-1}\left[\exp\left(-\frac{i\Delta x}{2k_0}(k_y^2+k_z^2)\right)\right.\\
&\left.\cdot\mathcal{F}\left[\exp\left(\frac{ik_0}{2}\int_x^{x+\Delta x/2}(\hat{n}^2(s)-1)ds\right)\boldsymbol{\Psi}(x)\right]\right].
\end{aligned}
$$

(5)

Above, $\mathcal{F}$ and $\mathcal{F}^{-1}$ denote 2D (discrete) Fourier and inverse Fourier transforms, respectively, and k_y and k_z are the discrete Fourier dual (spatial frequency) variables of y and z, respectively. Alternatively, discrete sine or cosine transforms may be used, depending on the boundary conditions

TABLE I. Notation: fields, indices, and operators referenced throughout the text.

Variables	Description
ψ	Continuous wave envelope
$\mathcal{Y}_j, \mathcal{Z}_j$	Continuous DO modes and coefficients of wave envelope
m_x, m_y, m_z	Number of discretized points in x, y, z
$\boldsymbol{\Psi}$	Discretized wave envelope with each range slice $\in \mathbb{C}^{m_y\times m_z}$
r	Rank of the reduced-order solution with $r \ll m_y, m_z$
$\mathcal{M}_r$	Manifold of rank-r, $m_y \times m_z$ matrices
$\boldsymbol{\Psi}_r$	Rank-r approximation to discretized wave envelope with each range slice $\in \mathcal{M}_r$
$\boldsymbol{Y}, \boldsymbol{Z}$	Matrix decomposition of any generic low-rank matrix (e.g., $\boldsymbol{Y}_{\boldsymbol{\Psi}_r}\boldsymbol{Z}_{\boldsymbol{\Psi}_r}^*$) with $\boldsymbol{Y} \in \mathbb{C}^{m_y\times r}$, $\boldsymbol{Z} \in \mathbb{C}^{m_z\times r}$
$\boldsymbol{Y}_{\boldsymbol{\Psi}_r}, \boldsymbol{Z}_{\boldsymbol{\Psi}_r}$	Matrix decomposition of $\boldsymbol{\Psi}_r = \boldsymbol{Y}_{\boldsymbol{\Psi}_r}\boldsymbol{Z}_{\boldsymbol{\Psi}_r}^* \in \mathcal{M}_r$
$\mathscr{P}_{\mathcal{M}_r}$	Projection operator that maps a matrix $\in \mathbb{C}^{m_y\times m_z}$ to the manifold of rank-r matrices $\mathcal{M}_r$
$\mathcal{R}_{\boldsymbol{\Psi}_r}(\Delta\boldsymbol{\Psi}_r)$	Retraction of $\Delta\boldsymbol{\Psi}_r$ at $\boldsymbol{\Psi}_r$ equal to $\boldsymbol{\Psi}_r + \mathscr{P}_{\mathcal{T}_{\boldsymbol{\Psi}_r}\mathcal{M}_r}\Delta\boldsymbol{\Psi}_r + \mathcal{O}(||\Delta\boldsymbol{\Psi}_r||^2)$
$\tilde{n}$	Continuous complex effective refractive index
A	Continuous reaction operator $\frac{ik_0}{2}(\tilde{n}^2-1)$
B	Continuous diffusion operator $\frac{i}{2k_0}\nabla_\perp^2$
$\hat{n}$	y-z discretized approximations to $\tilde{n}$
$\boldsymbol{D}$	Discretized, integrated diffusion operator $\exp\left(-\frac{i\Delta x}{2k_0}\left(k_y^2+k_z^2\right)\right)$ represented in $\mathbb{C}^{m_y\times m_z}$
$\boldsymbol{R}(x_0, x_1)$	Discretized, integrated reaction operator $\exp\left(\frac{ik_0}{2}\int_{x_0}^{x_1}(\hat{n}^2(s)-1)ds\right)$ represented in $\mathbb{C}^{m_y\times m_z}$
r_R	Rank of $\boldsymbol{R}$
$\boldsymbol{Y}_D, \boldsymbol{Z}_D$	Matrix decomposition of $\boldsymbol{D} = \boldsymbol{Y}_D\boldsymbol{Z}_D^* \in \mathbb{C}^{m_y\times 1}\times\mathbb{C}^{m_z\times 1}$
$\boldsymbol{Y}_R, \boldsymbol{Z}_R$	Matrix decomposition of $\boldsymbol{R} = \boldsymbol{Y}_R\boldsymbol{Z}_R^* \in \mathbb{C}^{m_z\times r_R}\times\mathbb{C}^{m_y\times r_R}$

imposed. Note that a second-order accurate approximation to $\int(\hat{n}^2(s)-1)ds$ may be used, e.g., the midpoint or trapezoidal rule. Typically, $\hat{n}$ is taken to be constant within the range step, so the integral is taken as the integrand multiplied by the step size (Hardin, 1973; Jensen *et al.*, 2011; Lin, 2019). Not shown are the zero-padding and truncation before and after Fourier-transforming via the 2/3 or 3/2 rule to avoid aliasing (Orszag, 1971); if aliasing is not a dominant source of error, this step may be skipped.

The splitting order of A and B may be swapped, and so another second-order SSF algorithm is

$$
\begin{aligned}
\boldsymbol{\Psi}(x+\Delta x) = \mathcal{F}^{-1}&\left[\exp\left(-\frac{i\Delta x}{4k_0}(k_y^2+k_z^2)\right)\right.\\
&\cdot\mathcal{F}\left[\exp\left(\frac{ik_0}{2}\int_x^{x+\Delta x}(\hat{n}^2(s)-1)ds\right)\right.\\
&\left.\left.\cdot\mathcal{F}^{-1}\left[\exp\left(-\frac{i\Delta x}{4k_0}(k_y^2+k_z^2)\right)\mathcal{F}[\boldsymbol{\Psi}(x)]\right]\right]\right].
\end{aligned}
$$

(6)

Note that if $\boldsymbol{\Psi}$ does not need to be saved at a step in range, we may avoid an inverse and forward Fourier transform and combine the first and last diffusion steps. In addition, though Eq. (5) generally has two fewer Fourier transforms, Eq. (6) becomes more efficient for a low-rank implementation, as will be discussed in Sec. II B.

B. Range-dynamical lr-SSF

The SSF algorithm is efficient largely due to the fast Fourier transform's (FFT's) $\mathcal{O}(m_ym_z\log(m_ym_z))$ complexity, where m_y and m_z are the number of points in the y and z grids, respectively. However, this operation becomes costly at even moderately high frequencies or large domains, as is often the case in ocean acoustics. To address this challenge, the number of degrees of freedom can be reduced via an approximation technique that, in the context of matrix differential equations, is called the dynamical low-rank approximation (DLRA) (Koch and Lubich, 2007). An analogous technique for PDEs in the context of continuous dynamics is called the DO equation (Sapsis and Lermusiaux, 2009; Ueckermann *et al.*, 2013). The DO reduction can be shown to be instantaneously optimal (Feppon and Lermusiaux, 2018a,b). With this DO decomposition, the memory constraint of storing every point in the fine meshes necessary to respect the Nyquist criterion will be avoided, and an integration scheme that scales sub-linearly with the number of points in the mesh will be developed.

In continuous space, one may decompose the solution to the governing PDE [Eq. (3)] by making the following ansatz (see Table I):

$$
\psi(x,y,z) = \sum_{j=1}^{\infty}\mathcal{Y}_j(y,x)\overline{\mathcal{Z}_j}(z,x). \tag{7}
$$

Here, $\overline{}$ denotes complex conjugation. Equation (7) simply indicates that the envelope function ψ may be decomposed as

J. Acoust. Soc. Am. **156** (4), October 2024

Aaron Charous and Pierre F. J. Lermusiaux 2905

the superposition of separable functions. This is always the case for L^2 functions, and indeed there exists a best approximation if we truncate the sum to r terms (Šimša, 1992). Such a decomposition is similar to that used in normal modes (Jensen *et al.*, 2011), but there are several important distinctions. First, the modes $\overline{\mathcal{Z}_j}$ in Eq. (7) as the coefficients $\mathcal{Y}_j$ are here functions of x; both $\mathcal{Y}_j$ and $\mathcal{Z}_j$ dynamically evolve in range. Second, the decomposition naturally handles slowly varying environmental range dependence without having to make approximations beyond those already made in deriving the parabolic wave equation. For normal modes to handle range-dependent environments (Ali and Lermusiaux, 2024a,b), one typically must use a coupled modes approach (Evans, 1983) and/or further neglect coupling using an adiabatic approximation (Pierce, 1965) where energy is not exchanged between different modes. Third, and importantly, the modes are not known *a priori*. Instead, the PDEs with the DO decomposition or DLRA dictate how to evolve the modes instantaneously in-range to best capture the solution at reduced order (Feppon and Lermusiaux, 2018a).

A discrete rank-r approximation, $\boldsymbol{\Psi}_r$, is a y-z discretization of the decomposition of the wave envelope $\boldsymbol{\Psi}$ in Eq. (7) truncated to rank-r,

$$\boldsymbol{\Psi}_r(x) = \sum_{j=1}^{r} \boldsymbol{Y}_{\boldsymbol{\Psi}_r,j}(x)\boldsymbol{Z}^*_{\boldsymbol{\Psi}_r,j}(x) = \boldsymbol{Y}_{\boldsymbol{\Psi}_r}(x)\boldsymbol{Z}^*_{\boldsymbol{\Psi}_r}(x). \qquad (8)$$

Assuming $\boldsymbol{\Psi}_r(x) \in \mathbb{C}^{m_y \times m_z}$, then $\boldsymbol{Y}_{\boldsymbol{\Psi}_r}(x) \in \mathbb{C}^{m_y \times r}$, $\boldsymbol{Z}_{\boldsymbol{\Psi}_r}(x) \in \mathbb{C}^{m_z \times r}$, $\boldsymbol{Y}_{\boldsymbol{\Psi}_r,j}(x)$, and $\boldsymbol{Z}_{\boldsymbol{\Psi}_r,j}(x)$ are the jth columns of $\boldsymbol{Y}_{\boldsymbol{\Psi}_r}(x)$ and $\boldsymbol{Z}_{\boldsymbol{\Psi}_r}(x)$, respectively, and $*$ denotes the conjugate transpose (see Table I). The quality of this approximation depends on r and also how quickly the singular values of $\boldsymbol{\Psi}$ decay. Empirically, solutions to the narrow-angle parabolic wave equation in ocean acoustics have rapid singular value decay, as will be shown in Sec. IV.

Now, an efficient method is obtained to evolve this low-rank representation in range. Let $\mathscr{P}_{\mathscr{M}_r}$ denote the operator that projects a matrix in the Euclidean space $\mathbb{C}^{m_y \times m_z}$ onto the manifold consisting of rank-r $m_y \times m_z$ matrices, $\mathscr{M}_r$. This operator maps a matrix that is potentially full-rank to its best rank-r approximation; it may be computed by taking the truncated singular value decomposition. Our two full-rank SSF schemes in Eqs. (5) and (6) are converted to lr-SSF schemes as

$$\boldsymbol{\Psi}_r(x + \Delta x)$$
$$= \mathscr{P}_{\mathscr{M}_r}\left\{ \exp\left(\frac{ik_0}{2}\int_{x+\Delta x/2}^{x+\Delta x}(\hat{n}^2(s)-1)ds\right) \right.$$
$$\cdot \mathcal{F}^{-1}\left[\exp\left(-\frac{i\Delta x}{2k_0}(k_y^2 + k_z^2)\right)\right.$$
$$\left.\left. \cdot\mathcal{F}\left\{\mathscr{P}_{\mathscr{M}_r}\left\{\exp\left(\frac{ik_0}{2}\int_{x}^{x+\Delta x/2}(\hat{n}^2(s)-1)ds\right)\boldsymbol{\Psi}_r(x)\right\}\right\}\right]\right\}$$
$$\qquad (9)$$

and

$$\boldsymbol{\Psi}_r(x + \Delta x)$$
$$= \mathcal{F}^{-1}\left[\exp\left(-\frac{i\Delta x}{4k_0}(k_y^2 + k_z^2)\right)\right.$$
$$\cdot \mathcal{F}\left[\mathscr{P}_{\mathscr{M}_r}\left\{\exp\left(\frac{ik_0}{2}\int_{x}^{x+\Delta x}(\hat{n}^2(s)-1)ds\right)\right.\right.$$
$$\left.\left.\cdot\mathcal{F}^{-1}\left[\exp\left(-\frac{i\Delta x}{4k_0}(k_y^2 + k_z^2)\right)\mathcal{F}[\boldsymbol{\Psi}_r(x)]\right]\right\}\right]\right]. \qquad (10)$$

The low-rank modifications include substituting in $\boldsymbol{\Psi}_r$ as our approximation of $\boldsymbol{\Psi}$ into the full-rank schemes and strategically placing projection operators, without which the rank of the approximation could grow precipitously. In Sec. III, these projection operators, their locations in Eqs. (9) and (10), and the retractions are discussed in detail.

III. RANGE-DYNAMICAL LR-SSF: ALGORITHMS AND ANALYSIS

In this section, algorithmic details of our range-dynamical lr-SSF schemes are presented and analyzed. Retractions are first introduced as computationally efficient approximations to the projection operator $\mathscr{P}_{\mathscr{M}_r}$. In particular, a rank-adaptive retraction is utilized so that the low-rank solution captures fine details in the simulation without incurring unnecessary computational costs as the rank changes with range. The next subsections (Secs. III A and III B) discuss how to compute the diffusion and reaction operators in the SSF schemes in a low-rank setting without reconstructing the solution at each step in range. Interpolating the refractive index is often required, and several strategies are proposed and compared. The last two subsections (Secs. III C and III D) describe the low-rank boundary conditions and computational cost compared to the classic full-rank SSF algorithm.

A. Low-rank integration via rank-adaptive retractions

Computing the truncated singular value decomposition every time step would be computationally expensive and prohibitive. For a full-rank $m_y \times m_z$ matrix with $m_z \leq m_y$, the singular value decomposition complexity scales as $\mathcal{O}(m_y m_z^2)$ (Trefethen and Bau, 1997). One may use approximations to $\mathscr{P}_{\mathscr{M}_r}$ such as the randomized singular value decomposition (Halko *et al.*, 2011), or one may use mappings back to the low-rank manifold called retractions (Absil and Oseledets, 2015). Retractions $\mathcal{R}_{\boldsymbol{\Psi}_r}(\Delta\boldsymbol{\Psi}_r)$ require a starting point on the low-rank manifold, $\boldsymbol{\Psi}_r$, and a direction to travel, $\Delta\boldsymbol{\Psi}_r$. To first-order,

$$\mathcal{R}_{\boldsymbol{\Psi}_r}(\Delta\boldsymbol{\Psi}_r) = \boldsymbol{\Psi}_r + \mathscr{P}_{\mathcal{T}_{\boldsymbol{\Psi}_r}\mathscr{M}_r}\Delta\boldsymbol{\Psi}_r + \mathcal{O}(||\Delta\boldsymbol{\Psi}_r||^2),$$

where $\mathscr{P}_{\mathcal{T}_{\boldsymbol{\Psi}_r}\mathscr{M}_r}$ denotes the operator that projects its argument onto the tangent space of the low-rank manifold at $\boldsymbol{\Psi}_r = \boldsymbol{Y}_{\boldsymbol{\Psi}_r}\boldsymbol{Z}^*_{\boldsymbol{\Psi}_r}$ (see Fig. 1). Second-order gradient-descent retractions would approximate the exact projection operator $\mathscr{P}_{\mathscr{M}_r}$ up to $\mathcal{O}(||\Delta\boldsymbol{\Psi}_r||^3)$, thus further reducing the projection-retraction error accumulation, which arises due to
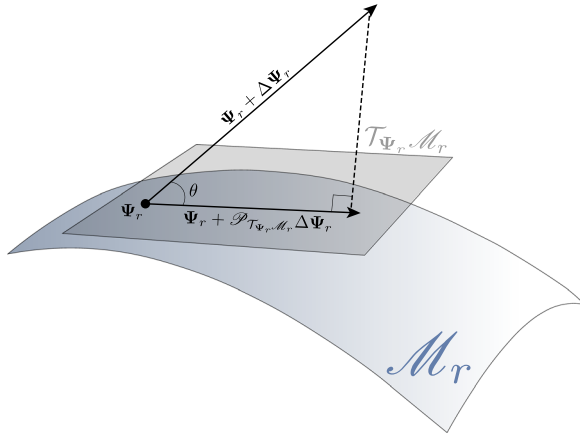
Aaron Charous and Pierre F. J. Lermusiaux

FIG. 1. (Color online) Starting from a point Ψ_r on the low-rank manifold $\mathcal{M}_r$, the PDE dynamics dictate the solution propagates in direction $\Delta\Psi_r$. To stay on the low-rank manifold, the dynamics are projected onto the tangent space, a first-order approximation to the nonlinear manifold. The angle θ gives information on the goodness of our low-rank approximation. If θ is large, one may choose to augment the rank of our approximation using our adaptive-rank integration scheme.

integration along a nonlinear manifold (Charous and Lermusiaux, 2023). For more information on retractions, we refer to Absil and Malick (2012), Absil and Oseledets (2015), Feppon and Lermusiaux (2018a,b, 2019), and Charous and Lermusiaux (2023, 2024) for acoustic examples.

At a high level, the projection operator $\mathscr{P}_{\mathcal{M}_r}$ and retractions $\mathcal{R}$ differ in that retractions require a starting point, i.e., an initial matrix (Ψ_r). As such, to implement Eq. (9) or (10), one takes

$$\mathscr{P}_{\mathcal{M}_r}(O[\Psi_r(x)]) \approx \mathcal{R}_{\Psi_r(x)}(O[\Psi_r(x)] - \Psi_r(x)),$$

where O is the operator respective to each lr-SSF algorithm. The details of the operators O are discussed in Sec. III B.

In this work, to compute $\mathcal{R}_{\Psi_r(x)}(O[\Psi_r(x)] - \Psi_r(x))$, the automatic, iterative rank-adaptive gradient-descent retractions from Charous and Lermusiaux (2024) are utilized, mainly because of their robustness to small singular values and convergence guarantees. These retractions employ Newton's method along the low-rank manifold to find the best low-rank approximation. They project onto the tangent space, then retract, then project onto the tangent space at the new point, then retract again, etc. At each iteration or stage, a first-order approximation to the manifold at one point is thus used, and not second- or higher-order approximations. A bird's eye summary of these retractions is given in Algorithm 1.

Walking through the algorithm, the first step is to calculate the angle between $(O[\Psi_r] - \Psi_r)$ and its projection onto the tangent space. If the angle is large, it indicates the dynamics depart the low-rank manifold quickly, so the rank should be augmented. If so, the randomized singular value decomposition (Halko *et al.*, 2011) is used to find the dominant modes of the residual between $(O[\Psi_r] - \Psi_r)$ and its tangent space projection. These modes are orthonormalized against the current subspace of Ψ_r and augmented to it.

ALGORITHM 1. Overview of automatic, iterative rank-adaptive gradient-descent retraction.

Require: $O: \mathbb{C}^{m_y \times m_z} \to \mathbb{C}^{m_y \times m_z}$, $\Psi_r \in \mathcal{M}_{r_1}$, $\theta^* \in [0, \pi/2]$, $\sigma^* \in [0, 1]$,
$\qquad r_{\text{inc}} \in \mathbb{Z}^+$, $r_{\text{max}} \in \mathbb{Z}^+$
Ensure: $\mathcal{R}_{\Psi_r}(O[\Psi_r] - \Psi_r) \in \mathcal{M}_{r_2}$
1:   $r_1 = \text{rank}(\Psi_r)$
2:   $\theta = \arccos\left(\dfrac{||\mathscr{P}_{\mathcal{T}_{\Psi_r}\mathcal{M}_r}(O[\Psi_r] - \Psi_r)||}{||O[\Psi_r] - \Psi_r||} \right)$ (see Fig. 1)
3:   **if** $r_1 < r_{\text{max}}$ and $\theta > \theta^*$ **then**
4:       $r_2 = \min(r_{\text{max}}, r_1 + r_{\text{inc}})$
5:       Augment the subspace of Ψ_r with left-most singular vectors of $(I - \mathscr{P}_{\mathcal{T}_{\Psi_r}\mathcal{M}_r})(O[\Psi_r] - \Psi_r)$ computed via the randomized SVD, see Charous and Lermusiaux (2024), alg. 4.1
6:   **end if**
7:   Obtain $\mathcal{R}_{\Psi_r}(O[\Psi_r] - \Psi_r)$: Use Newton's method on the low-rank manifold with robust, stable, optimal retractions until convergence. Start from Ψ_r in the direction of $(O[\Psi_r] - \Psi_r)$, see Charous and Lermusiaux (2024), alg. 3.2, Eqs. (4.2) and (4.4)
8:   **if** $\sigma_{\text{smallest}}(\Psi_r) < \sigma^*$ and the rank was not augmented **then**
9:       Truncate the rank of $\mathcal{R}_{\Psi_r}(O[\Psi_r] - \Psi_r)$ via an eigendecomposition of the coefficients' correlation matrix, see Charous and Lermusiaux (2024), alg. 4.1
10:      $r_2 = \text{rank}(\mathcal{R}_{\Psi_r}(O[\Psi_r] - \Psi_r))$
11: **end if**

Next, gradient descent is performed along the low-rank manifold in order to find the best low-rank approximation to $O[\Psi_r]$. During each step of the low-rank Newton's method, a retraction robust to small singular values is applied to map the matrix back to the low-rank manifold. This procedure is repeated until the newly found point $\mathcal{R}_{\Psi_r}(O[\Psi_r] - \Psi_r)$ stops changing within some threshold in the Frobenius norm. Once found, if the rank was not just augmented, the rank may be reduced if the smallest singular value of $\mathcal{R}_{\Psi_r}(O[\Psi_r] - \Psi_r)$ is beneath some user-specified threshold σ^*. This is accomplished by truncating the eigendecomposition of the low-rank matrix's coefficients' correlation matrix and then a corresponding rotation of the subspace. All of the numerical details of the algorithm may be found in Charous and Lermusiaux (2024).

B. Low-rank operators

Thus far, the operator O has served to abstractly describe either a diffusion $\boldsymbol{D}$ or reaction operator $\boldsymbol{R}$ in Eqs. (9) and (10). For concreteness, we now discuss the operators themselves, letting

$$\boldsymbol{D} \equiv \exp\left(-\frac{i\Delta x}{2k_0}(k_y^2 + k_z^2) \right),$$

$$\boldsymbol{R}(x_0, x_1) \equiv \exp\left(\frac{ik_0}{2} \int_{x_0}^{x_1} (\hat{n}^2(s) - 1) ds \right).$$

Above, the reaction operator is applied in the spatial domain while the diffusion operator is applied in the Fourier domain. Below, we rewrite Eqs. (9) and (10) with the matrix operators:

J. Acoust. Soc. Am. **156** (4), October 2024

Aaron Charous and Pierre F. J. Lermusiaux   2907

$$\Psi_r(x+\Delta x) = \mathscr{P}_{\mathcal{M}_r}\big\{ R(x+\Delta x/2, x+\Delta x)$$
$$\cdot \mathcal{F}^{-1}\big[D\mathcal{F}\big[\mathscr{P}_{\mathcal{M}_r}\{ R(x,x+\Delta x/2)\Psi_r(x)\}\big]\big]\big\},$$

(11)

$$\Psi_r(x+\Delta x) = \mathcal{F}^{-1}\Big[D^{\frac{1}{2}}\mathcal{F}\Big[\mathscr{P}_{\mathcal{M}_r}\big\{ R(x,x+\Delta x)$$
$$\cdot \mathcal{F}^{-1}\big[D^{\frac{1}{2}}\mathcal{F}[\Psi_r(x)]\big]\big\}\Big]\Big].$$

(12)

Fortunately, the diffusion operator is rank-1: By nature of the exponential function, it is separable in terms of the Fourier dual variables of y and z. As such, projecting back to the low-rank manifold is only required after applying the reaction operator.

Applying the reaction operator amounts to a Hadamard (elementwise) product in the discrete space. The rank of the reaction operator depends on $\hat{n}^2$. If the refractive index is high-rank, the projection following this step will be the bottleneck of the algorithm because the rank resulting from applying a Hadamard product is the product of the ranks of the multiplicands. Frequently, the reaction operator is low-rank: This is because environmental data are correlated and commonly available on a much coarser mesh than our fine computational mesh for Ψ or Ψ_r. In this case, one would like to interpolate the environmental parameters while restricting the rank of the reaction operator. However, interpolating $\hat{n}^2(x)$ directly and then forming the reaction operator would require re-projecting the reaction operator onto the low-rank manifold; for range-varying $\hat{n}$, this would be computationally costly to do at every range step.

There are several approaches to obtain the low-rank reaction operator. One is to first form the reaction operator on the coarse environmental grid. Then, nearest-neighbor interpolation may be applied. This is equivalent to doing nearest-neighbor interpolation of $\hat{n}^2(x)$ and then forming the reaction operator, but directly preserving the low-rank structure of the data. Note that one may interpolate over the columns of each of the reaction operator's low-rank factors Y_R

and Z_R in one dimension separately rather than having to crawl over the entire dense mesh (see Fig. 2). A second approach is to linearly interpolate the reaction operator. Linearly interpolating the low-rank factors in one dimension is also equivalent to two-dimensional (2D) linear interpolation over the reaction operator. However, this will induce artificial absorption or energy generation since the complex exponential nature of the reaction operator will be destroyed. A third approach would be to use nonlinear interpolation schemes on the reaction operator. This may also induce artificial absorption or energy generation, and the one-dimensional (1D) interpolation will not be equivalent to 2D interpolation.

A fourth entirely different approach is to interpolate, form, and truncate the reaction operator offline. This choice is beneficial when the environmental grid is dense and/or large. In this case, we may interpolate $\hat{n}^2$ directly in two dimensions using a potentially nonlinear method. For each range step, we may form the reaction operator and then truncate its rank via the truncated singular value decomposition (SVD), a randomized SVD, or retractions. Once this is precomputed, we may re-use it for different initial conditions, i.e., different pulse shapes and/or starting positions. Unless simulating low frequencies, the wavelength of our acoustic source is almost always much smaller than the length scale for which we have environmental data, so this offline process should be relatively cheap compared to the actual solve of the acoustic PE. Such offline environmental rank reductions are efficient and justified since the ocean is often low rank (Lermusiaux, 2001, 2006; Lermusiaux *et al.*, 2006). It is commonly what we employ, especially for environments assumed fixed during the fast acoustic propagation (Ali and Lermusiaux, 2024; Lermusiaux and Chiu, 2002; Lermusiaux *et al.*, 2002a; Lermusiaux *et al.*, 2002b; Lermusiaux *et al.*, 2010).

A discussion on truncating the rank of the reaction operator is provided in Charous (2023). The reaction operator is
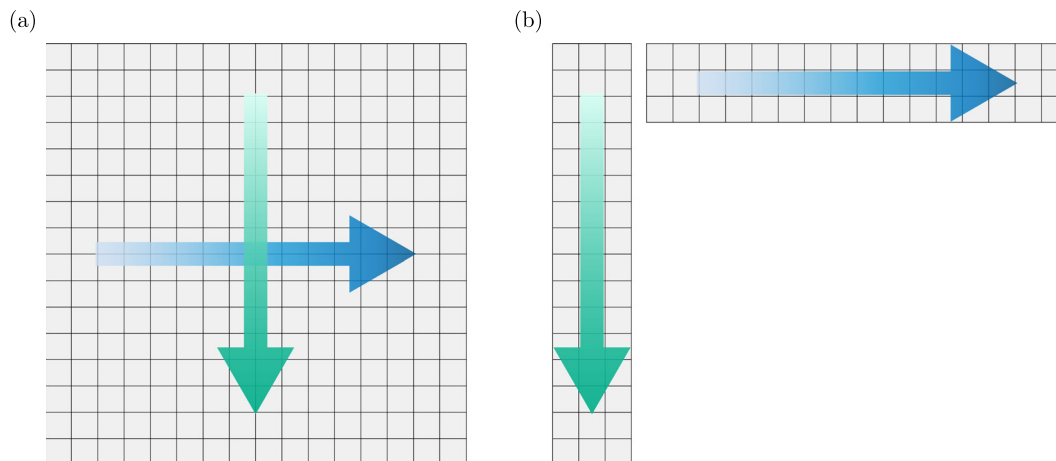

FIG. 2. (Color online) Many operations over a 2D grid, e.g., nearest-neighbor and linear interpolation as well as discrete Fourier transforms, are computed by sweeping across the rows and then columns (or vice versa) of the matrix. This is depicted in panel (a), and typically the sweeps along each dimension must be done serially. In contrast, a low-rank representation allows for parallel computation, which is depicted in panel (b). One may traverse the low-rank decomposition YZ^* without forming the large, dense matrix, offering large computational savings.

Aaron Charous and Pierre F. J. Lermusiaux

low-rank provided that $\hat{n}^2$ is low-rank and that Δx is small enough. The former condition is common as mentioned above. The latter condition was already required by the second-order SSF integrators in Eqs. (5) and (6) used to unroll steps 1–3 in Sec. II A. The worst case is if $\hat{n}^2 - 1$ is not low-rank, which could correspond to highly complex (e.g., random) media, almost white noise in space. In this case, reduced-order models are not fruitful, not even the dynamical low-rank approximation; using the full-rank dynamics is unavoidable.

In summary, four methods have been proposed to interpolate the refractive index from sparse environmental data to the fine resolution required to resolve the wavefield. The first and most straightforward one—using nearest-neighbor interpolation—is demonstrated in Sec. IV. Because its interpolant is piecewise constant and thus nonsmooth, artificial reflections may be induced, however. The other methods using non-constant interpolation may introduce artificial energy or absorption into the system. The fourth method that forms and reduces $\hat{n}^2$ offline may not always be feasible, but doing so when possible may yield the most physically correct and efficient solutions.

C. Low-rank boundary conditions

To impose absorbing boundary conditions, artificial absorption layers are added on all boundaries except for the pressure-release (Dirichlet-zero) boundary at the surface. An imaginary component is added to the complex refractive index in the absorbing boundary region. Abstractly, the *total* effective complex refractive index $\tilde{n}_{tot}$ may be written as

$$\tilde{n}_{tot}^2 = \tilde{n}^2(x,y,z) + ig(y) + ih(z).$$

g and h are some smooth, real function that are zero in the computational domain of interest and positive in the absorbing regions. In this case, the first half of a Gaussian peaking at the edge of the computational domain is used (Jensen *et al.*, 2011, Sec. 6.5.3). In the lr-SSF method, one could directly use $\hat{n}_{tot}$ as a discrete approximation to $\tilde{n}_{tot}$ in our reaction operator to incorporate the artificial absorption. However, as discussed before, interpolating this refractive index is not straightforward, and g and h need to be smooth to avoid artificial reflections, which would not be the case if using nearest-neighbor interpolation. Instead, the reaction operator $\boldsymbol{R}$ is separated as

$$\exp\left(\frac{ik_0}{2}\int_x^{x+\Delta x}(\hat{n}_{tot}^2(s)-1)ds\right)$$
$$= \exp\left(\frac{ik_0}{2}\int_x^{x+\Delta x}(\hat{n}^2(s)-1)ds\right)$$
$$\cdot \exp\left(-\frac{k_0\Delta x}{2}g(y)\right)\exp\left(-\frac{k_0\Delta x}{2}h(z)\right).$$

The first term of the right-hand side is the reaction term without artificial absorption, and implementation details

were discussed previously. The second and third terms are the artificial absorption. Because they are separable, they form a rank-1 operator, and so one may easily apply it without increasing the rank of the solution.

D. Computational cost

Now, the computational advantages offered by the lr-SSF method in Eqs. (11) and (12) are discussed. First, consider the computational complexity of the full-rank algorithms in Eqs. (5) and (6). As before, assume that $\boldsymbol{\Psi} \in \mathbb{C}^{m_y \times m_z}$. Applying the reaction and diffusion operators requires $\mathcal{O}(m_y m_z)$ operations, and the FFT requires $\mathcal{O}(m_y m_z \log(m_y m_z))$ operations. Consequently, the total leading computational complexity of the full-rank SSF algorithm is

$$\mathcal{O}(m_y m_z \log(m_y m_z)). \tag{13}$$

Next, assume $\boldsymbol{\Psi}_r \in \mathscr{M}_r$ and the low-rank reaction operator $\boldsymbol{R} = \boldsymbol{Y}_R \boldsymbol{Z}_R^*$ has rank r_R. Throughout, assume that any argument's operator is decomposed in low-rank form as $\boldsymbol{YZ}^*$. Applying the low-rank diffusion operator $\boldsymbol{D} = \boldsymbol{Y}_D \boldsymbol{Z}_D^*$ involves a rank-1 multiplication, i.e., an elementwise product of $\boldsymbol{Y}_D \in \mathbb{C}^{m_y}$ and $\boldsymbol{Z}_D \in \mathbb{C}^{m_z}$ with every column of $\boldsymbol{Y} \in \mathbb{C}^{m_y \times r}$ and $\boldsymbol{Z} \in \mathbb{C}^{m_z \times r}$, respectively. Consequently, this operation has complexity $\mathcal{O}(r(m_y + m_z))$. Applying the reaction operator amounts to taking the elementwise product of every pair of columns in $\boldsymbol{Y}_R$ and $\boldsymbol{Y}$ as well as $\boldsymbol{Z}_R$ and $\boldsymbol{Z}$. This step takes $\mathcal{O}(rr_R(m_y + m_z))$ operations. Next, one must project the resulting matrix of rank rr_R back to $\mathscr{M}_r$. From Charous and Lermusiaux (2024), the retraction takes $\mathcal{O}(r(r + r_R)(m_y + m_z))$ operations. Finally, the FFT may be computed along every column of $\boldsymbol{Y}$ and $\boldsymbol{Z}$ in parallel (see Fig. 2), which will take $\mathcal{O}(r(m_y \log(m_y) + m_z \log(m_z)))$ operations. In total, our lr-SSF algorithm has computational complexity

$$\mathcal{O}(r(r + r_R)(m_y + m_z) + r(m_y \log(m_y) + m_z \log(m_z))). \tag{14}$$

For simplicity, consider the case when $m_y = m_z$ and propagation in 3D physical space. The total number of points in our grid for $\boldsymbol{\Psi}$ is $M \equiv m_y^2$ and the full-rank algorithm scales log-linearly in the total number of points, i.e., as $\mathcal{O}(M \log M)$. In contrast, from Eq. (14), our low-rank algorithm scales as $\mathcal{O}(r\sqrt{M} \log\sqrt{M})$. Furthermore, if we have m_x points in range, the storage of the full-rank solution involves $m_x M$ values, whereas the low-rank approximation only requires storing $m_x \sqrt{M}$ values. This is a dramatic improvement and facilitates the solution of much larger 3D problems. Figure 3 compares and contrasts the computational scaling between full-rank and low-rank algorithms by timing the algorithms for one step of integration with random data.

This analysis also gives us insight into the dominating computational costs of each algorithm. In the full-rank algorithm, Eq. (13) indicates that the bottleneck is the FFT, and so Eq. (5) is typically more efficient than Eq. (6). In contrast, the reaction and projection/retraction operators are the

J. Acoust. Soc. Am. **156** (4), October 2024

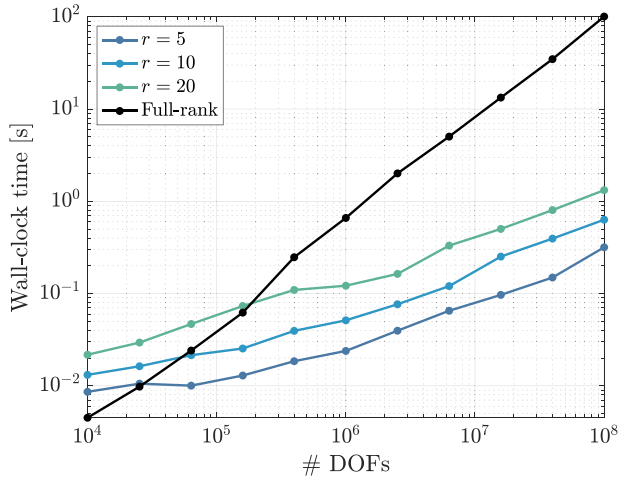Aaron Charous and Pierre F. J. Lermusiaux 2909

FIG. 3. (Color online) Comparison of the computational complexity of the full-rank split-step Fourier algorithm [Eq. (6)] and its low-rank variant [Eq. (10)] on random data. The wall-clock time of integrating one step in range with random environmental parameters and initial conditions is displayed. For the low-rank variant, we truncate the rank of the solution to $r = 5$, 10, and 20. By varying the number of points in y and z, $M = m_y^2 = m_z^2$, we observe $\mathcal{O}(M \log M)$ scaling for the full-rank algorithm and $\mathcal{O}(r\sqrt{M} \log \sqrt{M})$ scaling for the low-rank algorithm. For moderately sized problems, the low-rank algorithms are already orders of magnitude faster.

algorithmic bottlenecks for the low-rank method in Eq. (12); the first term in Eq. (14) typically dominates the second because the logarithmic growth is so slow. As a result, Eq. (10) is typically more efficient than Eq. (9).

IV. NUMERICAL EXPERIMENTS

To showcase the efficacy of the dynamical lr-SSF method, we solve the narrow-angle parabolic wave equation in two 3D computational domains in Massachusetts Bay at both 75 and 750 Hz (Fig. 4). The ocean fields are from realistic high-resolution data-assimilative simulations for the region shown on Fig. 4(a). The first acoustic domain [Fig. 4(b)] is oriented latitudinally across the northwest corner of Stellwagen Bank, while the second [Fig. 4(c)] is oriented longitudinally along a double-forked canyon. Next, the ocean field inputs and the acoustic initial conditions, boundary conditions, discretization, and parameters are described. The results of 3D numerical simulations in each domain are then presented and analyzed.

A. Ocean conditions

For the ocean density and sound speed fields, the MIT Multidisciplinary Simulation, Estimation, and Assimilation Systems (MSEAS) primitive-equation ocean modeling system is used (Haley *et al.*, 2015; Haley and Lermusiaux, 2010). It was set up for August to September 2019. The numerical modeling domain has a high 3D resolution, with 333 m second-order finite volumes in the horizontal and 100 optimized levels in the vertical. The bathymetry is from the 3-arc sec U.S. Geological Survey (USGS) Gulf of Maine digital elevation model (Twomey and Signell, 2013). For
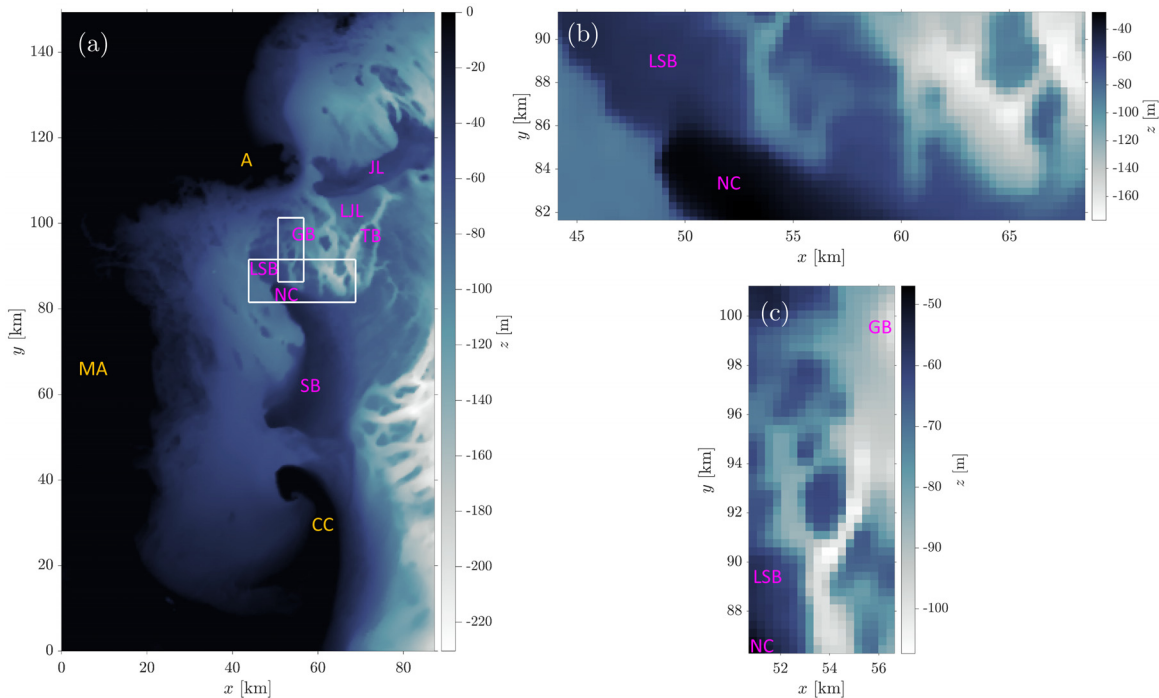

FIG. 4. (Color online) (a) Bathymetry in the Massachusetts Bay domain used by the MSEAS ocean primitive-equation simulations, overlaid with the two 3D acoustics computational domains. (b) First acoustic domain: bathymetry in the latitudinal 10 km × 25 km domain from Lower Stellwagen Bank, over Northwest Corner, to the Canyons south of Gloucester Basin. (c) Second acoustic domain: bathymetry in the longitudinal 6 km × 15 km domain along the two-forked canyon (down to 90 m east and to 120 m west), just east of Lower Stellwagen Bank, north of Northwest Corner, and south-southeast of Gloucester Basin. Note the depth color bar limits differ for each panel. Land (orange): Massachusetts (MA), Cape Ann (A), and Cape Cod (CC). Bathymetry features (magenta): Stellwagen Bank (SB), Northern Corner (NC), Lower Stellwagen Bank (LSB), Gloucester Basin (GB), Tillies Bank (TB), Lower Jeffreys Ledge (LJL), and Jeffreys Ledge (JL).

Aaron Charous and Pierre F. J. Lermusiaux

tidal forcing, the TPXO8-Atlas tides (Egbert and Erofeeva, 2002, 2024) are employed after updates for our high-resolution bathymetry and coastlines (Logutov and Lermusiaux, 2008). For atmospheric forcing, the 3 km North American Mesoscale Forecast System (NAM) from the National Centers for Environmental Prediction (NCEP) [National Centers for Environmental Prediction (NCEP), 2023] is used. The sub-tidal initial and boundary conditions are initialized by downscaling from 1/12° analyses from the HYbrid Coordinate Ocean model (HYCOM) (Cummings and Smedstad, 2013; HYCOM Consortium, 2023), after optimized updates for higher-resolution coastlines and bathymetry (Haley *et al.*, 2015) and corrections using *in situ* data from the National Marine Fisheries Service (NMFS) collected on August 28, 2019 (National Marine Fisheries Service, 2019). The resulting MSEAS ocean simulation was run from August 11 to September 13, 2019. It was validated against independent data, e.g., National Oceanic and Atmospheric Administration National Data Buoy Center (NOAA NDBC) buoy data [National Data Buoy Center (NDBC), 2019], and demonstrated forecast skill. For more on the oceanography, we refer to Haley *et al.* (2020) and Ali *et al.* (2023).

The 3D ocean density and sound speed fields of 00Z August 14, 2019, are used for the acoustics computations. The median of our 3D sound speed data is taken to be the reference speed c_0. Sound speed field sections in our two acoustic domains are depicted in Fig. 5. In the first domain, Figs. 4(b) and 5(a)–5(c), the internal tides and the meandering coastal current with eddies just before the steep Northwest Corner and the internal tides above the Lower Stellwagen Bank are visible. Further in range, the sound speed field variability shows internal tides and waves mostly generated in response to the two main canyons, as well as

similar waves and eddies that occur around the two seamounts [see Figs. 5(a)–5(c)]. In the second domain [Figs. 4(c) and 5(d)–5(f)], the double-fork canyon environment with the edge of the Lower Stellwagen Bank followed by several short seamounts leads to the generation of internal tides, topographic waves, and mixing zones, all of which are visible in our MSEAS ocean primitive-equation simulation [see Figs. 5(d)–5(f)].

We stress that we are interested in evaluating the lr-SFF in comparison to the full-rank SFF and in finding out if the lr-SFF solution is accurate under such realistic ocean conditions. The reduction in computational cost without loss of accuracy compared to the classic SFF is the main result we seek to demonstrate. The Massachusetts Bay ocean environment is simulated at high resolution: second-order schemes, 333 m horizontal grid, and 100 vertical levels are not coarse for coastal ocean simulations (e.g., Deleersnijder *et al.*, 2010; Deleersnijder and Lermusiaux, 2008). However, we are not studying the effects of small-scale ocean processes on 3D acoustics. This would require even higher ocean resolution (e.g., less than 100 m in the horizontal) and non-hydrostatic physics (Ueckermann, 2014; Ueckermann and Lermusiaux, 2016). Of course, our acoustics spatial resolutions are much higher than our ocean ones due to the acoustic wavelengths.

B. Initial and boundary conditions

The parabolic wave equations are initialized using a Gaussian starter with a standard deviation equal to 1 over the reference wavenumber, $1/k_0$. The method of images is used to ensure the pressure-release boundary condition at the surface is enforced. Absorbing boundary conditions are used as described in Sec. III.
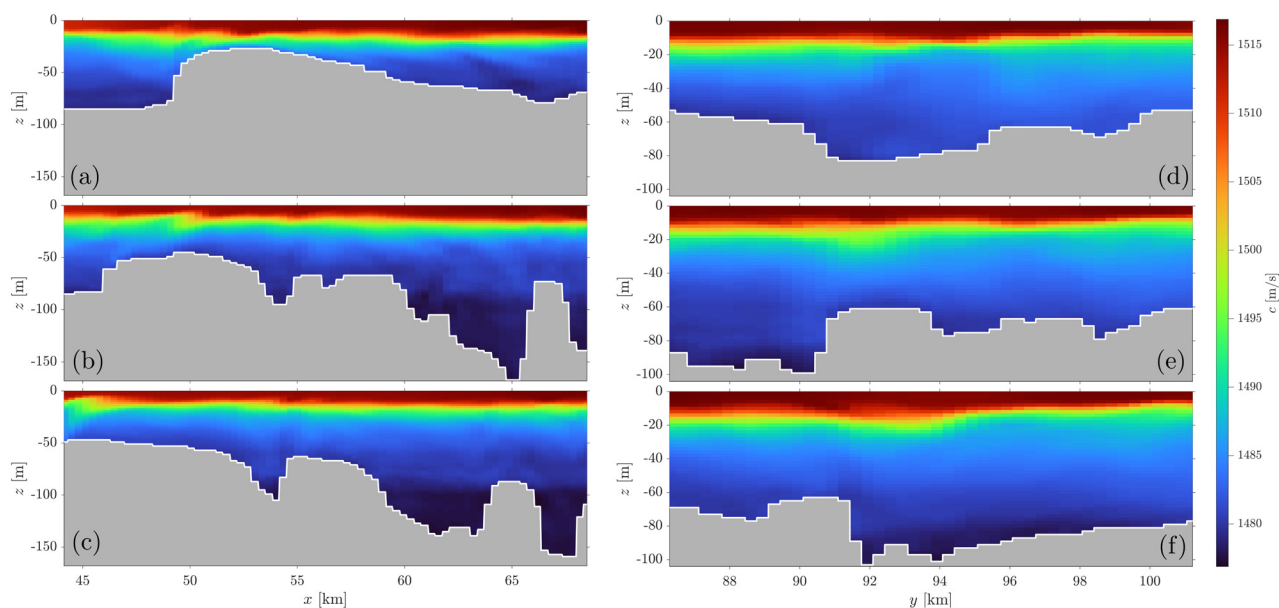

FIG. 5. (Color online) MSEAS primitive-equation data-assimilative analysis of the 3D sound speed field for 00Z August 14, 2019, after interpolation onto our acoustic grids. (a)–(c) First domain: latitudinal vertical slices of sound speed for fixed $y \approx 82\,303$, $86\,501$, and $90\,266$ m, respectively. (d)–(f) Second domain: Longitudinal vertical slices of sound speed for fixed $x \approx 52\,031$, $53\,677$, and $54\,994$ m, respectively.

C. Acoustic spatial discretization and parameters

In each acoustic computational domain, a discrete sine series is used as our pseudospectral basis in the vertical direction z and a Fourier basis in the transverse direction (y for the first domain and x for the second). To avoid aliasing, the PDE is solved on two grids: A dense grid is used in the spatial domain when applying the reaction operator, and a coarse grid is used in the frequency domain when applying the diffusion operator. Compared to the coarse grid, the dense grid has twice as many points in y/x and one more than twice as many points in z. Note that a padding ratio of only 3/2 rather than 2 is required to avoid aliasing; however, using a ratio of 3/2 requires the coarse grid to have an even number of points in y/x and an odd number of points in z so that the resulting dense grid overlaps with the coarse grid. To make our scheme compatible with differently sized grids, 3/2 is rounded up to a pad ratio of 2.

Second-order central differences are used to compute the gradients of density in calculating the complex effective refractive index [Eq. (4)]. The density discontinuity is smoothed along the sea floor using the method in Tappert (1977) via a hyperbolic tangent function with characteristic length $L = 2/k_0$. A fluid bottom with absorption $\alpha^{(\lambda)} = 0.5\,\mathrm{dB}/\lambda$ is used. The artificial absorption layers add an additional $0.35\,\mathrm{dB}/\lambda$ for 663.73 m in y and 984 m in z in application 1 and $3.5\,\mathrm{dB}/\lambda$ for 329.31 m in x and 98 m in z in application 2; the seemingly random absorption layer lengths are due to different discrete resolutions in y and z and different characteristic wavelengths in the two applications.

D. Application 1: 75 Hz across Northwest Corner on Stellwagen Bank

The first 3D numerical simulations propagate energy latitudinally in the positive x direction in Fig. 4, approximately west to east, at a frequency of 75 Hz. At this mid-low frequency, the full-rank 3D solution is computed using the classic SSF algorithm and compared with our low-rank 3D algorithm. A source is placed at $(x_0, y_0, z_0) = (43\,797.8, 86\,500, -20)$ m. On the coarse grid, there are $m_x = 5025$ grid-points in x, $m_y = 4454$ in y, and $m_z = 2362$ in z, corresponding to $\Delta x = 4.8505$ m, $\Delta y = 2.4594$ m, and $\Delta z = 0.61537$ m. On the dense grid, there are 8908 grid-points in y and 4725 in z, corresponding to $\Delta y = 1.2297$ m and $\Delta z = 0.25013$ m. The full rank of the numerical solution is $\min(m_y, m_z) = 2362$.

Figure 6 illustrates the rapid singular value decay of the density-reduced pressure of the full-rank 3D solution of this first application halfway through the range of the simulation. Already at rank-2, over 99% of the energy in the Frobenius norm is recovered. At rank-8, over 99.9% of the energy is recovered. As a result, the DLRA is able to capture the full-rank solution extremely well.

In all figures, the transmission loss is normalized by the maximum solution value and is computed as $20\log_{10}(|p|/\max|p|)$.
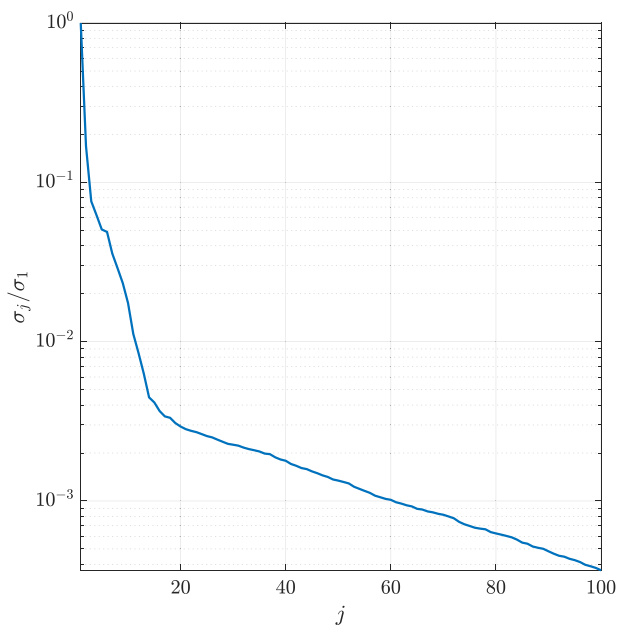

FIG. 6. (Color online) Application 1: first 100 singular values of full-rank 3D density-reduced pressure (without absorption layer) at $x \approx 56\,311$ m, halfway through the simulation.

Figure 7 shows the 3D transmission loss fields of the low-rank and full-rank solutions along three vertical slices and after depth-averaging. It is remarkable that the rank-5 solution captures the features of the full-rank solution so well. All of the solutions show energy bouncing off of the sea surface and sea bottom. In addition, when the acoustic wave reaches a sea ridge that is about two wavelengths (40 m) from the surface, the acoustic energy is quickly attenuated, indicating the DLRA respects the wave physics. Nevertheless, the rank-5 solution seems to decay faster than the full-rank solution in some regions and slower in others. The adaptive-rank solution recovers some of the detail lost and more closely matches the full-rank solution.

To better contrast the solutions, we show the difference in transmission loss between the low-rank and full-rank solutions in Fig. 8. At first glance, the error appears substantial. Why then do the solutions look so similar in Fig. 7? This is because the error is almost entirely in regions where the acoustic pressure is very close to zero. In areas where the acoustic energy is even moderately high, the DLRA appears to be extremely accurate.

To explain this discrepancy, consider the following example. If the full-rank solution has a value of $\sim 10^{-12}$ at a point and our low-rank approximation has a value of $\sim 10^{-9}$ at the same point, the difference plot will show 60 dB of error. However, at that point, the full-rank and low-rank solutions will be below -180 dB from the reference, so they will both appear black in Fig. 7.

This phenomenon points more broadly to how our range-dynamical low-rank approximation operates. Every time our system is projected onto the low-rank manifold, the residual between our system state and its low-rank approximation is minimized *in the Frobenius norm*. Consequently,

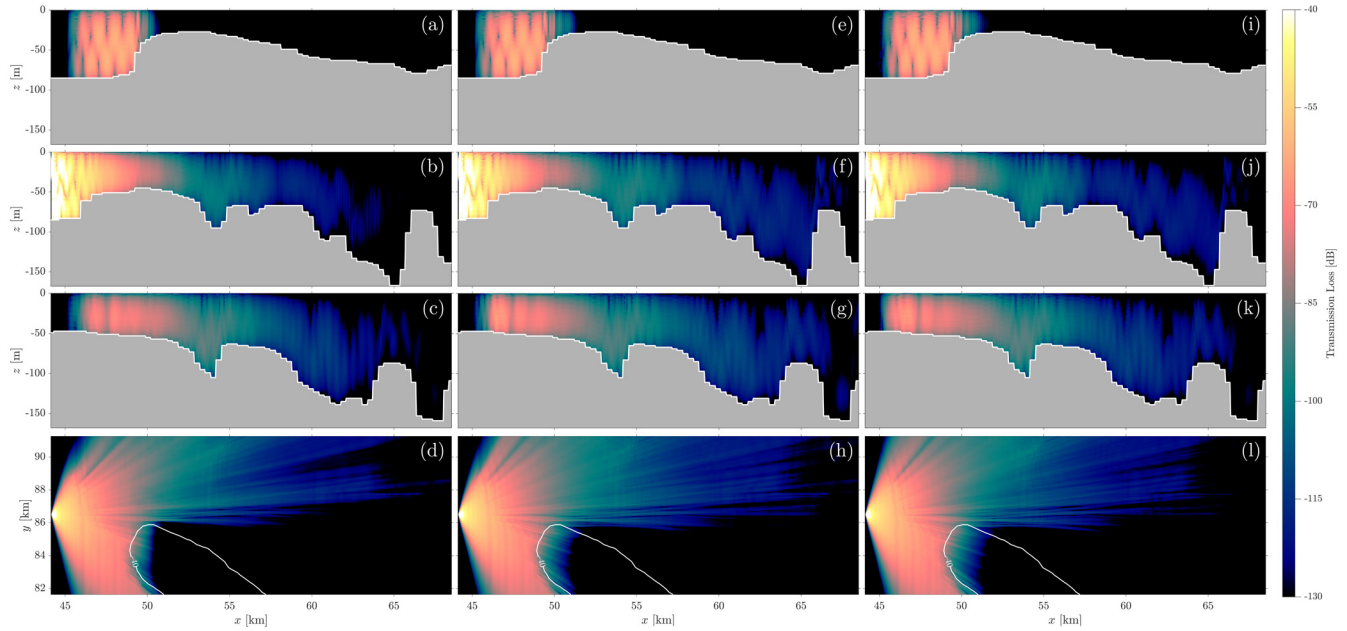Aaron Charous and Pierre F. J. Lermusiaux

FIG. 7. (Color online) Application 1: 3D transmission loss fields of the low rank-5 (a)–(d), adaptive-rank (e)–(h), and full-rank (i)–(l) solutions. First three rows show vertical slices of the solutions at $y \approx 82\,303$, $86\,501$, and $90\,266$ m overlaid with bathymetry. Last row: horizontal depth-averaged transmission loss fields overlaid with the $z = -40$ m isobath.

the relative error in areas where p is very small is orders of magnitude larger than where p is comparatively large. Typically, the low-rank approximation does not capture enough of the low energy in the sediment and misappropriates/redistributes degrees of freedom to other parts of the computational domain where the energy is much larger. A potential remedy could be developing retractions that minimize a weighted norm or a different norm that
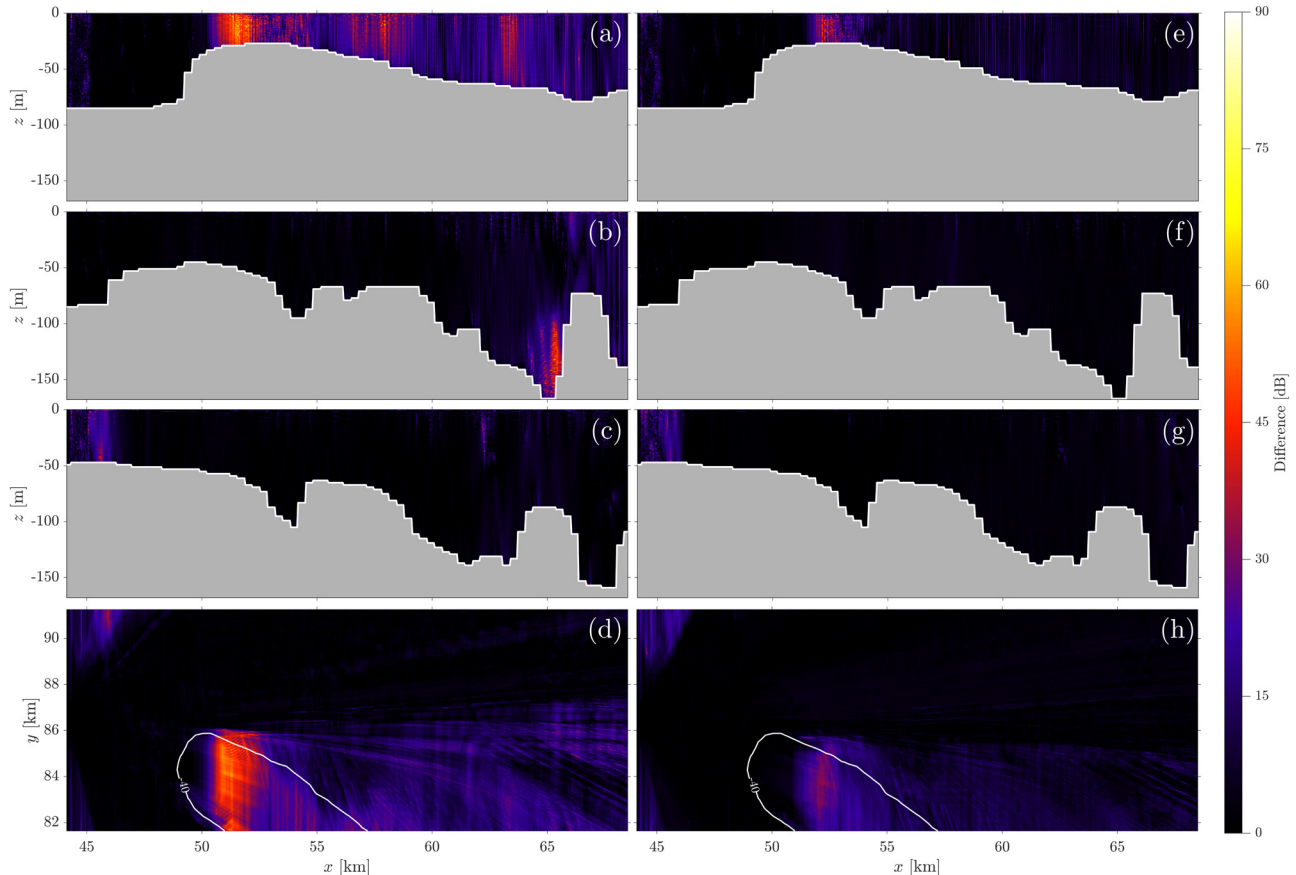

FIG. 8. (Color online) Application 1: 3D difference fields of the rank-5 (a)–(d) and adaptive-rank (e)–(h) approximations with the full-rank solution corresponding to Fig. 7.

takes into account matrices with elements that span multiple orders of magnitude or minimize relative instead of absolute error. This would, however, lead to larger absolute errors elsewhere. With that said, in most applications, minimizing the Frobenius norm in the DLRA is appropriate since, experimentally, the areas in which p is comparatively small are in the sediment and/or potentially at values beneath measurement noise, so our approximation provides valuable and accurate predictions.

Finally, we show that the lr-SSF method successfully captures not only the transmission loss but also the phase φ of the pressure solution. Figure 9 compares the solutions of the lr-SSF with that of the classical full-rank SSF. Figure 9(a) shows the difference in phase $|\Delta\varphi|$ as a function of range, weighted by quadratic pressure,

$$\frac{\int |p(x,y,z)|^2 |\varphi_{\text{fr}}(x,y,z) - \varphi_{\text{lr}}(x,y,z)| dy dz}{\int |p(x,y,z)|^2 dy dz}.$$

Since intensity is $|p|^2/\rho c$ and energy is $|p|^2/\rho c^2$ (Jensen *et al.*, 2011), the norm above may be interpreted as an energy- or intensity-weighted norm (since if ρ and c variations in the transverse plane are null, the denominators of intensity and energy cancel out of the integrals). Results show that all low-rank numerical solutions (rank-5, rank-10, and rank-adaptive) have very small phase errors. Though the rank-5 solution accumulates more error at the end of the simulation, the rank-10 and rank-adaptive solutions both closely match the full-rank phase. Figures 9(b)–9(d) show vertical slices at range 12.5 km of the full-rank intensity field, full-rank phase field, and phase difference between the low-rank-adaptive and full-rank fields, respectively. From

Fig. 9(d), we observe that the phase difference between the low-rank-adaptive and full-rank solutions is significant for small y. Fortunately, the intensity field of Fig. 9(b) shows that this phase error is essentially entirely in regions of very low intensity, which is consistent with the transmission loss error field (Figs. 7 and 8). Ideally, the phase error should be small everywhere, but in areas of very low acoustic energy, the phase of the solution tends to be physically unimportant. This behavior of prioritizing accuracy in areas of high energy arises since the lr-SSF method minimizes errors in the Frobenius norm.

E. Application 2: 750 Hz along the double-forked canyon east of Lower Stellwagen Bank

Our second 3D numerical simulations propagate energy longitudinally in the positive y direction, approximately south to north, at 750 Hz. At this higher frequency, a full-rank solution is not feasible on a desktop or even a reasonably-sized cluster due to the memory requirements. As a result, only dynamical low-rank approximations are computed in application 2. The source is placed at $(x_0, y_0, z_0) = (53\,677, 86\,284, -85)$ m. On the coarse grid, we use $m_x = 30\,360$ grid-points in x, $m_y = 26\,775$ in y, and $m_z = 4882$ in z, resulting in $\Delta x = 0.49191$ m, $\Delta y = 0.24599$ m, and $\Delta z = 0.061537$ m. The dense grid has $53\,550$ grid-points in y and 9765 in z, resulting in $\Delta y = 0.12299$ m and $\Delta z = 0.030309$ m. The full rank of the numerical solution is $\min(m_y, m_z) = 4882$.

Vertical slices in the 3D transmission loss fields are shown in Fig. 10 for the rank-5, rank-10, and adaptive-rank solutions. Although the full-rank solution is not available to serve as a reference, observe that the solutions are converging; the rank-10 solution is much more similar to the adaptive-rank solution than
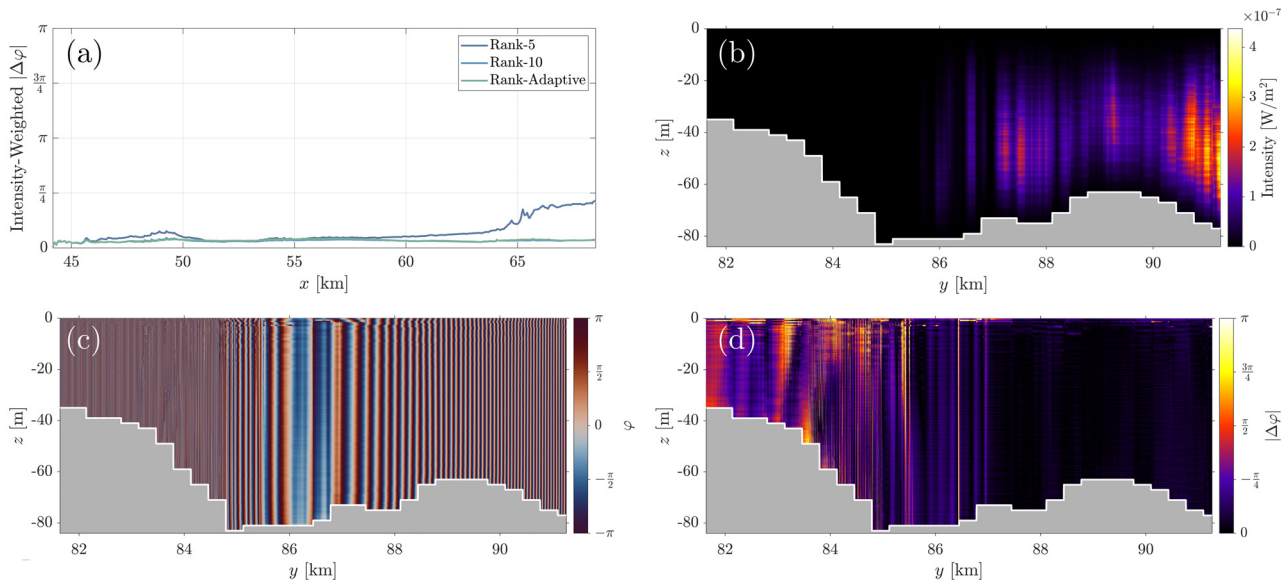

FIG. 9. (Color online) Application 1: phase error between low- and full-rank SSF pressure solutions. (a) Energy-/intensity-weighted phase error integrated within the transverse (cross-range) plane and plotted as a function of range, x. (b)–(d) Vertical slices after approximately 12.5 km of propagation in range, at $x \approx 56.31$ km: (b) intensity of the full-rank solution, (c) phase of the pressure of the full-rank solution, and (d) phase difference between the low adaptive-rank and full-rank solutions.

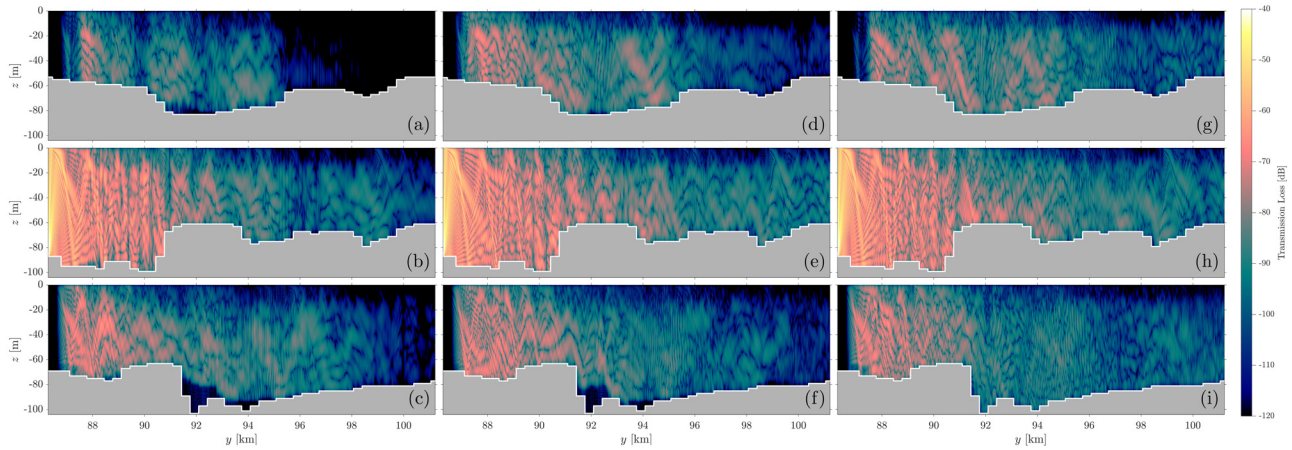Aaron Charous and Pierre F. J. Lermusiaux

FIG. 10. (Color online) Application 2: 3D transmission loss fields of the rank-5 (a)–(c), rank-10 (d)–(f), and adaptive-rank (g)–(i) solutions along vertical slices at $x \approx 52\,031$, $53\,677$, and $54\,994$ m, overlaid with bathymetry.

the rank-5 solution. In this more complicated 3D environment and a higher frequency (with more grid points in our computational domain), the rank-5 and rank-10 approximations do not always follow the bathymetry as closely as in the first application. The two fixed-rank solutions also underestimate the energy propagation in 3D at longer ranges, especially the rank-5 solution in Figs. 10(a)–10(c). These are all features of being underresolved in rank. Overall, these results provide some evidence that our adaptive-rank solution is a very good approximation to the full-rank solution and may serve as our reference. This will be further discussed later.

Figure 11 shows horizontal maps of the range-dynamical low-rank 3D transmission loss fields at depths $z = -60$ and $z = -65$ m. The coarse, block-like nature of the solution is because nearest-neighbor interpolation is used for the bathymetry, which translates into a coarse, block-like transmission loss. At all ranks, the energy is significantly attenuated by the bathymetry. However, the higher-rank approximations hug the bathymetry more closely, as was already noticed in Fig. 10.

Figure 12 shows deeper horizontal maps of the transmission loss fields at $z = -70$ and $z = -80$ m. Here, the full features of the canyon are present. The energy closely follows areas in which the sea floor is deeper than the horizontal map. This application demonstrates the true 3D nature of acoustic wave physics. If one were to simulate only 2D propagation along a vertical slice of the domain, the energy would quickly be blocked. In reality, the acoustic energy snakes its way in 3D through the double-forked canyon and around short seamounts, modifying the sound propagation to the Gloucester Basin. We note that such 3D bathymetric effects are also captured in the prior shallower maps but are logically not as visible (e.g., acoustic energy present behind seamounts for the rank-10 and especially adaptive-rank solutions in Fig. 11).

F. Discussions: Computational costs and adaptive rank

The computational costs and requirements are now analyzed for the two applications and their solutions of varied rank sizes. The properties and performance of the rank-adaptive schemes are also discussed.

In Tables II and III, the run times and memory requirements are enumerated for low fixed-rank, low adaptive-rank, and full-rank solutions in each computational domain. All simulations completed for the two applications presented in this work were run using the same central processing unit (CPU) (i9-9900, 8 cores up to 4.9 GHz; Intel, Santa Clara, CA) and random access memory (RAM) (4X16GB DDR4 2666 MHz), without parallelization. In application one (Table II), a $45\times$ speedup is observed for the rank-5 solution compared to the full-rank solution, and it only requires 1.39% of the memory. The rank-10 solution sees a $19\times$ speedup and uses 2.78% of the memory. The adaptive-rank solution sees an $8.5\times$ speedup and uses 3.5% of the memory; note that the adaptive-rank solution may be sped up further by increasing the threshold θ^*, at which the rank is augmented (see Fig. 1).

In application 2, the full-rank solution is not computed. With our selected resolution, each step in range operates over a $53\,550 \times 9765$ complex-valued grid, amounting to about 8.4 GB of data. With 30 360 steps in range, computing the solution would be extremely slow, and saving the solution at the same resolution as described in Table III would require 4.45 terabytes. From this, the rank-5 solution only uses 0.187% of the full-rank memory. The rank-10 and adaptive-rank solutions only use 0.373% and 0.688% of the full-rank memory, respectively.

Our rank-adaptive scheme (Sec. III A) allows updating the rank at each discrete range step of the range-dynamical lr-SSF method. This is in general needed because the optimal rank is not known *a priori* and the rank should increase or decrease on the fly in response to the PE variability in range. In our present applications, when the angle between the system dynamics and the projection of the dynamics onto the low-rank manifold's tangent space exceeds a threshold of $\theta^* = 0.1$ rad, the system rank is augmented by 1. If the low-rank approximation becomes ill-conditioned, we truncate the rank of the system to keep at least 99% of

J. Acoust. Soc. Am. **156** (4), October 2024

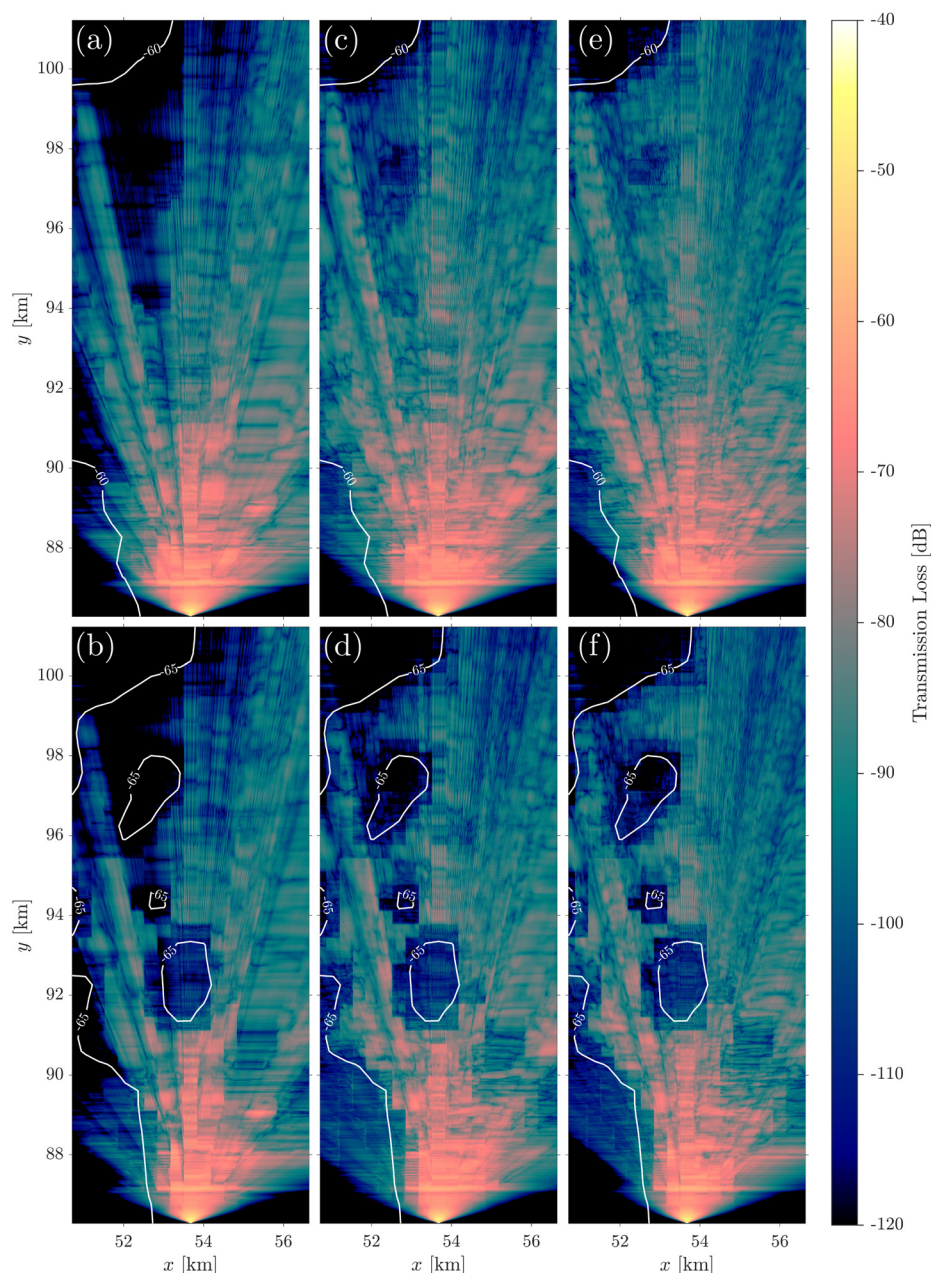Aaron Charous and Pierre F. J. Lermusiaux   2915

FIG. 11. (Color online) Application 2: 3D transmission loss fields of the rank-5 (a) and (b), rank-10 (c) and (d), and adaptive-rank (e) and (f) solutions at the horizontal depths of $z = -60$ m (first row) and $z = -65$ m (second row) overlaid with their respective isobaths.

the energy in the Frobenius norm. For further details, see Algorithm 1 in Sec. III A and Charous and Lermusiaux (2024).

Figure 13 depicts how the rank of the rank-adaptive solution adapts to the range-dependent environment and acoustics PE. In each application, the solution starts as rank-1 due to the Gaussian initial conditions. The rank grows as the acoustic wave propagates through heterogeneous media. In the first application [Fig. 13(a)] the rank stabilizes between 10 and 15; this is not known *a priori* and is discovered by the adaptive-rank gradient-descent retraction from Charous and Lermusiaux (2024). Specifically, the rank rapidly reaches about 10–14, then increases as acoustic waves reach the Lower Stellwagen Bank and especially the steep Northwest Corner and the strong internal tides. The rank then decays back to about 9–12 to re-increase again to 17–18 as waves leave the Northwest Corner and propagate across the western branch of the double-fork Canyon. Subsequently, the rank stabilizes back to 10–13 to slowly increase with range to about 15.

In the second application [Fig. 13(b)], the rank increases with range at a rate similar to that of the first application but stabilizes only at larger values between 20 and 25. This indicates that the higher frequency coupled with the complicated canyon environment with internal tides and topographic waves require a larger rank. Indeed, once strong internal tides and the effects of the short seamount are felt at the double-fork (see Figs. 4 and 5), the rank rapidly increases around $y = 92$ km and subsequently does not decay anymore.

V. CONCLUSION

The parabolic wave equation is much more computationally efficient than solving the acoustic wave or Helmholtz

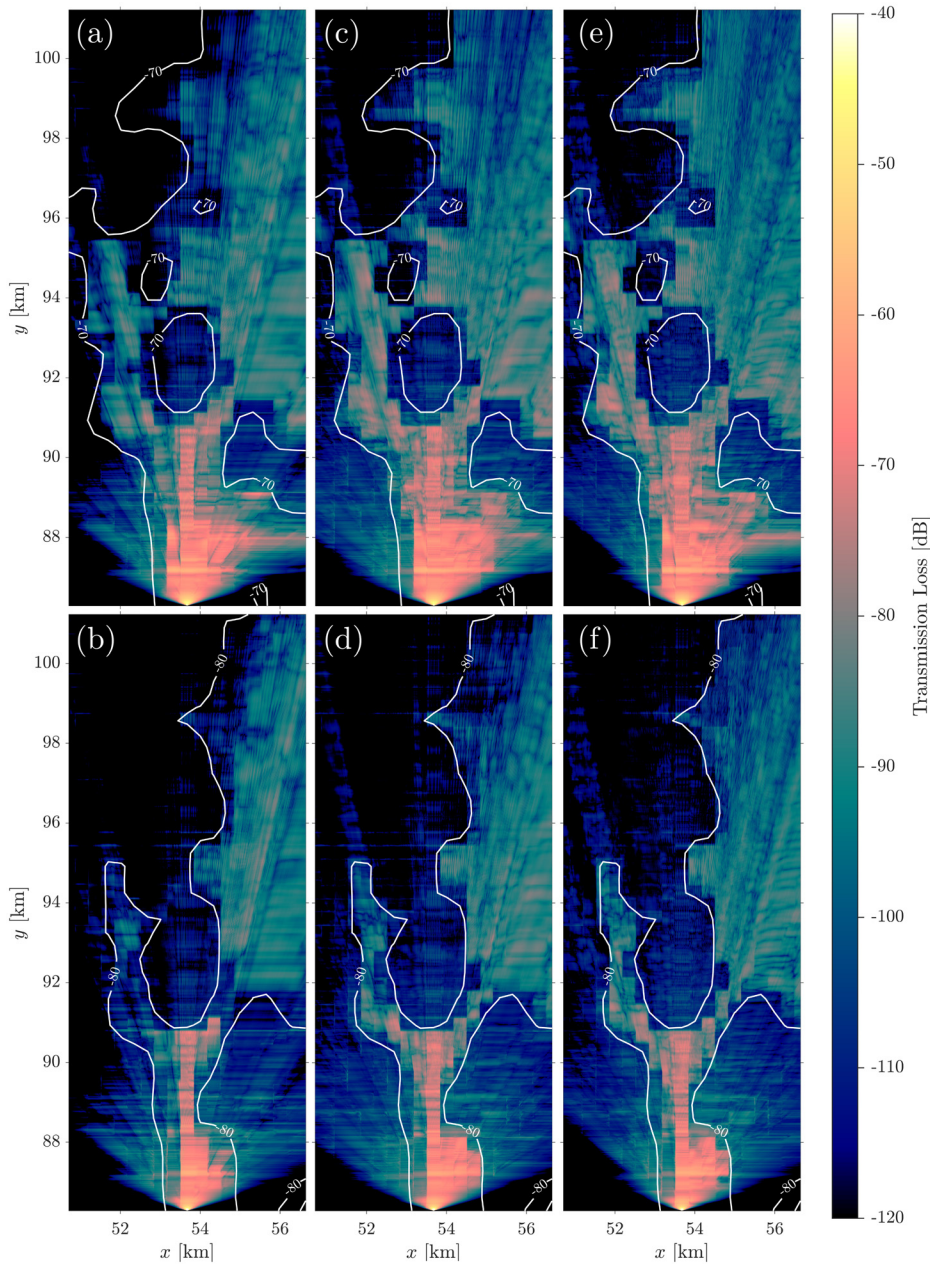Aaron Charous and Pierre F. J. Lermusiaux

FIG. 12. (Color online) Application 2: 3D transmission loss fields of the rank-5 (a) and (b), rank-10 (c) and (d), and adaptive-rank (e) and (f) solutions at the horizontal depths of $z = -70$ m (first row) and $z = -80$ m (second row) overlaid with their respective isobaths.

equations. However, large 3D computational domains and/or high frequencies still pose challenges due to the dense mesh required to resolve acoustic waves. Building off the familiar SSF method, a novel range-dynamical lr-SSF method is developed to optimally reduce the parabolic wave equation. Using a range-dynamical separation of variables in the transverse directions and making a DLRA, the Nyquist criterion and high resolution are still respected, but redundant degrees of freedom are removed from the dynamical system. We incorporate retractions as approximate projection operators to prevent the dimensionality of the reduced-order solution from growing exponentially with range and introduce

TABLE II. Application 1: run times and memory requirements to compute the low fixed-rank, low adaptive-rank, and full-rank solutions (75 Hz across Northwest Corner on Stellwagen Bank).[a]

Parameter	Rank-5	Rank-10	Adaptive-rank	Full
Run time (min)	11.0	25.1	57.9	495.8
Memory (GB)	0.217	0.433	0.538	15.6

[a]Every eight range steps are stored, but the absorbing boundary regions are not, amounting to 629 grid points in x, 3914 in y, and 395 in z.

TABLE III. Application 2: run times and memory requirements to compute the low fixed-rank and adaptive-rank solutions (750 Hz along the double-forked canyon east of Lower Stellwagen Bank).[a]

Parameter	Rank-5	Rank-10	Adaptive-rank
Run time (min)	142.4	311.2	1855.9
Memory (GB)	8.31	16.6	30.6

[a]Every eight range steps are stored, but the absorbing boundary regions are not, amounting to 3795 grid points in x, 26 775 in y, and 4882 in z.
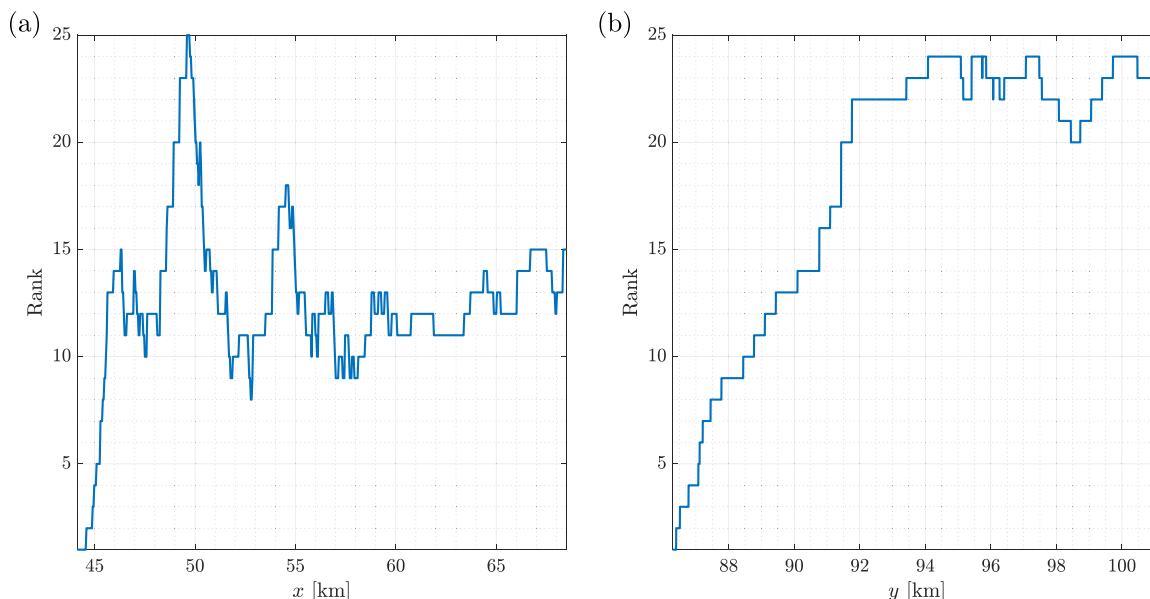
FIG. 13. (Color online) Adaptive rank as a function of range in applications 1 (a) and 2 (b).

rank-adaptive retractions to adjust the rank with range for better accuracy and efficiency. While the classic SSF scales log-linearly, the lr-SSF scales sub-linearly with the number of classical degrees of freedom in the dense mesh. Consequently, this algorithm can offer solution times orders of magnitude faster while requiring minimal storage (depending on the domain size and frequency).

Each operator in our low-rank algorithms was analyzed, and its computational complexity was derived. The dominating cost among all operators in the lr-SSF method is the projection/retraction operator required in each step in range rather than the Fourier transforms in the full-rank SSF method. Because of the data structure of a low-rank matrix, common operations such as matrix multiplications and Fourier transforms become much more efficient at low rank.

Finally, the range-dynamical lr-SSF method was employed at frequencies of 75 and 750 Hz on realistic high-resolution data-assimilative ocean fields with internal tides, eddies, and jets around Stellwagen Bank in Massachusetts Bay. Two geometries with seamounts and canyons, across and along the Bank, were considered, along with different source locations and frequencies. Our results confirm the convergence with the rank of the subspace and the efficiency of the rank-adaptive retractions. Run times and memory requirements were compared for the low-rank and full-rank algorithms as well as the accuracy of the low-rank approximations. Furthermore, the rank-adaptive algorithm automatically finds a suitable rank for the solution without *a priori* knowledge of the environment. No matter how truncated, in the sense of quadratic pressure, the range-dynamical lr-SSF best respects the local wave physics, and acoustic energy propagates naturally.

In the future, there are many avenues for new applications and improvements to the methodology. Studying the long-range effects of non-hydrostatic ocean physics on 3D

acoustics is promising (Duda *et al.*, 2019; Duda *et al.*, 2014; Robinson and Lermusiaux, 2004). One could include stochastic models of uncertain and smaller ocean scales (Charous and Lermusiaux, 2021; Lermusiaux, 2006; Lermusiaux *et al.*, 2020a; Lermusiaux *et al.*, 2020b) and obtain probabilistic lr-SFF simulations. Bayesian inversion and learning may then be possible (Ali *et al.*, 2019; Lermusiaux, 2007; Lu and Lermusiaux, 2021). An integration scheme may be developed for the wide-angle parabolic wave equation (Halpern and Trefethen, 1988; Lin *et al.*, 2013). In addition, generalizing this work to cylindrical coordinates, solving on even larger domains, and computing on high-performance computer clusters may yield regional or even global ocean acoustic simulations that were hitherto intractable. In strongly range-dependent environments, we could also incorporate backscattering (Collins and Evans, 1992). Furthermore, the absorbing boundary region is somewhat wasteful, so we may consider implementing a perfectly matched layer (Berenger, 1994). Last, one may consider different norms to minimize when projecting/retracting back onto the low-rank manifold. As it is, the Frobenius norm is locally minimized in range. However, a norm that minimizes relative error rather than absolute error may be beneficial, and a projection operator that conserves energy in the Frobenius rather than the spectral norm (as the truncated SVD preserves the spectral norm) may better respect the physics.

ACKNOWLEDGMENTS

Aaron Charous and Pierre F. J. Lermusiaux

AUTHOR DECLARATIONS
Conflict of Interest

The authors have no conflicts to disclose.

DATA AVAILABILITY

The data that support the findings of this study are available from the corresponding author upon reasonable request.

Absil, P.-A., and Malick, J. (**2012**). "Projection-like retractions on matrix manifolds," SIAM J. Optim. **22**(1), 135–158.

Absil, P.-A., and Oseledets, I. V. (**2015**). "Low-rank retractions: A survey and new results," Comput. Optim. Appl. **62**(1), 5–29.

Ali, W. H., Bhabra, M. S., Lermusiaux, P. F. J., March, A., Edwards, J. R., Rimpau, K., and Ryu, P. (**2019**). "Stochastic oceanographic-acoustic prediction and Bayesian inversion for wide area ocean floor mapping," in *OCEANS 2019 MTS/IEEE SEATTLE*, Seattle, WA (IEEE, New York), pp. 1–10.

Ali, W. H., Charous, A., Mirabito, C., Haley, P. J., Jr., and Lermusiaux, P. F. J. (**2023**). "MSEAS-ParEq for ocean-acoustic modeling around the globe," in *OCEANS 2023 IEEE/MTS U.S. Gulf Coast*, Biloxi, MS (IEEE, New York), pp. 1–10.

Ali, W. H., and Lermusiaux, P. F. J. (**2024a**). "Dynamically orthogonal narrow-angle parabolic equations for stochastic underwater sound propagation. Part I: Theory and schemes," J. Acoust. Soc. Am. **155**(1), 640–655.

Ali, W. H., and Lermusiaux, P. F. J. (**2024b**). "Dynamically orthogonal narrow-angle parabolic equations for stochastic underwater sound propagation. Part II: Applications," J. Acoust. Soc. Am. **155**(1), 656–672.

Berenger, J.-P. (**1994**). "A perfectly matched layer for the absorption of electromagnetic waves," J. Comput. Phys. **114**(2), 185–200.

Botseas, G., Lee, D., and King, D. (**1987**). "FOR3D: A computer model for solving the LSS three-dimensional wide angle wave equation," NUSC TR 7943, U.S. Naval Underwater Systems Center, New London, CT.

Castor, K., and Sturm, F. (**2008**). "Investigation of 3D acoustical effects using a multiprocessing parabolic equation based algorithm," J. Comput. Acoust. **16**(02), 137–162.

Cervený, V. (**2001**). *Seismic Ray Theory* (Cambridge University Press, Cambridge, UK), Vol. 110.

Charous, A. (**2023**). "Dynamical reduced-order models for high-dimensional systems," Ph.D. thesis, Massachusetts Institute of Technology, Cambridge, MA.

Charous, A., and Lermusiaux, P. F. J. (**2021**). "Dynamically orthogonal differential equations for stochastic and deterministic reduced-order modeling of ocean acoustic wave propagation," in *OCEANS 2021, San Diego—Porto*, San Diego, CA (IEEE, New York), pp. 1–7.

Charous, A., and Lermusiaux, P. F. J. (**2023**). "Dynamically orthogonal Runge–Kutta schemes with perturbative retractions for the dynamical low-rank approximation," SIAM J. Sci. Comput. **45**(2), A872–A897.

Charous, A., and Lermusiaux, P. F. J. (**2024**). "Stable rank-adaptive dynamically orthogonal Runge–Kutta schemes," SIAM J. Sci. Comput. **46**, A529–A560.

Collins, M. D. (**1993**). "A split-step Padé solution for the parabolic equation method," J. Acoust. Soc. Am. **93**(4), 1736–1742.

Collins, M. D., Cederberg, R. J., King, D. B., and Chin-Bing, S. A. (**1996**). "Comparison of algorithms for solving parabolic wave equations," J. Acoust. Soc. Am. **100**(1), 178–182.

Collins, M. D., and Evans, R. B. (**1992**). "A two-way parabolic equation for acoustic backscattering in the ocean," J. Acoust. Soc. Am. **91**(3), 1357–1368.

Collins, M. D., and Siegmann, W. L. (**2019**). *Parabolic Wave Equations with Applications* (Springer, Berlin).

Cummings, J. A., and Smedstad, O. M. (**2013**). *Variational Data Assimilation for the Global Ocean* (Springer, Berlin), pp. 303–343.

Deleersnijder, E., Legat, V., and Lermusiaux, P. F. J. (**2010**). "Multi-scale modelling of coastal, shelf and global ocean dynamics," Ocean Dyn. **60**(6), 1357–1359.

Deleersnijder, E., and Lermusiaux, P. F. J. (**2008**). "Multi-scale modeling: Nested-grid and unstructured-mesh approaches," Ocean Dyn. **58**(5–6), 335–336.

DiNapoli, F. R., and Deavenport, R. L. (**1980**). "Theoretical and numerical Green's function field solution in a plane multilayered medium," J. Acoust. Soc. Am. **67**(1), 92–105.

Duda, T. F. (**2006**). "Initial results from a Cartesian three-dimensional parabolic equation acoustical propagation code," Technical Report WHOI-2006-14, Woods Hole Oceanographic Institution, Woods Hole, MA.

Duda, T. F., Lin, Y.-T., Newhall, A. E., Helfrich, K. R., Lynch, J. F., Zhang, W. G., Lermusiaux, P. F. J., and Wilkin, J. (**2019**). "Multiscale multiphysics data-informed modeling for three-dimensional ocean acoustic simulation and prediction," J. Acoust. Soc. Am. **146**(3), 1996–2015.

Duda, T. F., Lin, Y.-T., Newhall, A. E., Helfrich, K. R., Zhang, W. G., Badiey, M., Lermusiaux, P. F. J., Colosi, J. A., and Lynch, J. F. (**2014**). "The 'Integrated Ocean Dynamics and Acoustics' (IODA) hybrid modeling effort," in *Proceedings of the International Conference on Underwater Acoustics—2014 (UA2014)*, pp. 621–628, available at https://scholar.google.com/scholar?cluster=5677702977423602800&hl=en&as_sdt=0,22.

Egbert, G. D., and Erofeeva, S. Y. (**2002**). "Efficient inverse modeling of barotropic ocean tides," J. Atmos. Ocean. Technol. **19**(2), 183–204.

Egbert, G. D., and Erofeeva, S. Y. (**2024**). OTIS: OSU Tidal Inversion, https://www.tpxo.net/otis.

Evans, R. B. (**1983**). "A coupled mode solution for acoustic propagation in a waveguide with stepwise depth variations of a penetrable bottom," J. Acoust. Soc. Am. **74**(1), 188–195.

Ewing, W. M., Jardetzky, W. S., Press, F., and Beiser, A. (**1957**). "Elastic waves in layered media," Phys. Today **10**(12), 27–28.

Feppon, F., and Lermusiaux, P. F. J. (**2018a**). "Dynamically orthogonal numerical schemes for efficient stochastic advection and Lagrangian transport," SIAM Rev. **60**(3), 595–625.

Feppon, F., and Lermusiaux, P. F. J. (**2018b**). "A geometric approach to dynamical model-order reduction," SIAM J. Matrix Anal. Appl. **39**(1), 510–538.

Feppon, F., and Lermusiaux, P. F. J. (**2019**). "The extrinsic geometry of dynamical systems tracking nonlinear matrix projections," SIAM J. Matrix Anal. Appl. **40**(2), 814–844.

Haley, P. J., Jr., Agarwal, A., and Lermusiaux, P. F. J. (**2015**). "Optimizing velocities and transports for complex coastal regions and archipelagos," Ocean Model. **89**, 1–28.

Haley, P. J., Jr., Gupta, A., Mirabito, C., and Lermusiaux, P. F. J. (**2020**). "Towards Bayesian ocean physical-biogeochemical-acidification prediction and learning systems for Massachusetts Bay," in *Global Oceans 2020: Singapore–U.S. Gulf Coast*, Biloxi, MS (IEEE, New York), pp. 1–9.

Haley, P. J., Jr., and Lermusiaux, P. F. J. (**2010**). "Multiscale two-way embedding schemes for free-surface primitive equations in the 'Multidisciplinary Simulation, Estimation and Assimilation System,'" Ocean Dyn. **60**(6), 1497–1537.

Halko, N., Martinsson, P.-G., and Tropp, J. A. (**2011**). "Finding structure with randomness: Probabilistic algorithms for constructing approximate matrix decompositions," SIAM Rev. **53**(2), 217–288.

Halpern, L., and Trefethen, L. N. (**1988**). "Wide-angle one-way wave equations," J. Acoust. Soc. Am. **84**(4), 1397–1404.

Hardin, R. (**1973**). "Applications of the split-step Fourier method to the numerical solution of nonlinear and variable coefficient wave equations," SIAM Rev. **15**, 423.

Heaney, K. D., and Campbell, R. L. (**2016**). "Three-dimensional parabolic equation modeling of mesoscale eddy deflection," J. Acoust. Soc. Am. **139**(2), 918–926.

HYCOM Consortium (**2023**). "HYbrid Coordinate Ocean Model (HYCOM)," https://hycom.org (Last viewed April 9, 2019).

Ide, J. M., Post, R. F., and Fry, W. J. (**1947**). "The propagation of underwater sound at low frequencies as a function of the acoustic properties of the bottom," J. Acoust. Soc. Am. **19**(1), 283.

Jardetzky, W. S. (**1953**). "Period equation for an n-layered halfspace and some related questions," Technical Report on Seismology 29, Lamont Geological Observatory of Columbia University, Palisades, NY.

J. Acoust. Soc. Am. **156** (4), October 2024

Aaron Charous and Pierre F. J. Lermusiaux   2919

Jensen, F. B., Kuperman, W. A., Porter, M. B., Schmidt, H., and Tolstoy, A. (**2011**). *Computational Ocean Acoustics* (Springer, Berlin), Vol. 794.

Koch, O., and Lubich, C. (**2007**). "Dynamical low-rank approximation," SIAM J. Matrix Anal. Appl. **29**(2), 434–454.

Kutschale, H. W. (**1973**). "Rapid Computation by Wave Theory of Propagation Loss in the Arctic Ocean," CU-8-73, Technical Report 8, Lamont-Doherty Geological Observatory of Columbia University, Palisades, NY.

Lee, D., Schultz, M. H., and Siegmann, W. (**1995**). *Numerical Ocean Acoustic Propagation in Three Dimensions* (World Scientific, Singapore).

Leontovich, M. A., and Fock, V. A. (**1946**). "Solution of the problem of propagation of electromagnetic waves along the earth's surface by the method of parabolic equation," J. Phys. USSR **10**(1), 13–23.

Lermusiaux, P. F. J. (**2001**). "Evolving the subspace of the three-dimensional multiscale ocean variability: Massachusetts Bay," J. Mar. Syst. **29**(1), 385–422.

Lermusiaux, P. F. J. (**2006**). "Uncertainty estimation and prediction for interdisciplinary ocean dynamics," J. Comput. Phys. **217**(1), 176–199.

Lermusiaux, P. F. J. (**2007**). "Adaptive modeling, adaptive data assimilation and adaptive sampling," Phys. D: Nonlinear Phenom. **230**(1), 172–196.

Lermusiaux, P. F. J., and Chiu, C.-S. (**2002**). "Four-dimensional data assimilation for coupled physical-acoustical fields," in *Acoustic Variability, 2002*, edited by N. G. Pace and F. B. Jensen (Kluwer Academic Press, Amsterdam), pp. 417–424.

Lermusiaux, P. F. J., Chiu, C.-S., Gawarkiewicz, G. G., Abbot, P., Robinson, A. R., Miller, R. N., Haley, P. J., Jr., Leslie, W. G., Majumdar, S. J., Pang, A., and Lekien, F. (**2006**). "Quantifying uncertainties in ocean predictions," Oceanography **19**(1), 90–105.

Lermusiaux, P. F. J., Chiu, C.-S., and Robinson, A. R. (**2002a**). "Modeling uncertainties in the prediction of the acoustic wavefield in a shelfbreak environment," in *Proceedings of the 5th International Conference on Theoretical and Computational Acoustics*, Beijing China, edited by E.-C. Shang, Q. Li, and T. F. Gao (World Scientific Publishing Co., Singapore), pp. 191–200.

Lermusiaux, P. F. J., Haley, P. J., Jr., Mirabito, C., Ali, W. H., Bhabra, M., Abbot, P., Chiu, C.-S., and Emerson, C. (**2020a**). "Multi-resolution probabilistic ocean physics-acoustic modeling: Validation in the New Jersey continental shelf," in *Global Oceans 2020: Singapore–U.S. Gulf Coast*, Biloxi, MS (IEEE, New York), pp. 1–9.

Lermusiaux, P. F. J., Mirabito, C., Haley, P. J., Jr., Ali, W. H., Gupta, A., Jana, S., Dorfman, E., Laferriere, A., Kofford, A., Shepard, G., Goldsmith, M., Heaney, K., Coelho, E., Boyle, J., Murray, J., Freitag, L., and Morozov, A. (**2020b**). "Real-time probabilistic coupled ocean physics-acoustics forecasting and data assimilation for underwater GPS," in *Global Oceans 2020: Singapore–U.S. Gulf Coast*, Biloxi, MS (IEEE, New York), pp. 1–9.

Lermusiaux, P. F. J., Robinson, A. R., Haley, P. J., and Leslie, W. G. (**2002b**). "Advanced interdisciplinary data assimilation: Filtering and smoothing via error subspace statistical estimation," in *OCEANS '02 MTS/IEEE*, Biloxi, MS (IEEE, New York), pp. 795–802.

Lermusiaux, P. F. J., Xu, J., Chen, C.-F., Jan, S., Chiu, L., and Yang, Y.-J. (**2010**). "Coupled ocean–acoustic prediction of transmission loss in a continental shelfbreak region: Predictive skill, uncertainty quantification, and dynamical sensitivities," IEEE J. Ocean. Eng. **35**(4), 895–916.

Lichte, H. (**1919**). "On the influence of horizontal temperature stratification of seawater on the range of underwater sound signals," Physikalische Z. (17), 385–389.

Lin, Y.-T. (**2019**). "Three-dimensional boundary fitted parabolic-equation model of underwater sound propagation," J. Acoust. Soc. Am. **146**(3), 2058–2067.

Lin, Y.-T., Duda, T. F., and Newhall, A. E. (**2013**). "Three-dimensional sound propagation models using the parabolic-equation approximation and the split-step Fourier method," J. Comput. Acoust. **21**(1), 1250018.

Lin, Y.-T., Porter, M. B., Sturm, F., Isakson, M. J., and Chiu, C.-S. (**2019**). "Introduction to the special issue on three-dimensional underwater acoustics," J. Acoust. Soc. Am. **146**(3), 1855–1857.

Logutov, O. G., and Lermusiaux, P. F. J. (**2008**). "Inverse barotropic tidal estimation for regional ocean applications," Ocean Model. **25**(1–2), 17–34.

Lu, P., and Lermusiaux, P. F. J. (**2021**). "Bayesian learning of stochastic dynamical models," Phys. D: Nonlinear Phenom. **427**, 133003.

McLachlan, R. I., and Quispel, G. R. W. (**2002**). "Splitting methods," Acta Numerica **11**, 341–434.

National Centers for Environmental Prediction (NCEP) (**2023**). "The North American Mesoscale forecast system (NAM)," https://www.ncei.noaa.gov/products/weather-climate-models/north-american-mesoscale (Last viewed July 20, 2023).

National Data Buoy Center (NDBC) (**2019**). "National Data Buoy Center," https://www.ndbc.noaa.gov/ (Last viewed 2023).

National Marine Fisheries Service (**2019**). "New England/Mid-Atlantic: Science," https://www.nefsc.noaa.gov/HydroAtlas/ (Last viewed 2023).

Oliveira, T. C., Lin, Y.-T., and Porter, M. B. (**2021**). "Underwater sound propagation modeling in a complex shallow water environment," Front. Mar. Sci. **8**, 751327.

Orszag, S. A. (**1971**). "On the elimination of aliasing in finite-difference schemes by filtering high-wavenumber components," J. Atmos. Sci. **28**(6), 1074–1074.

Pekeris, C. L. (**1948**). "Theory of propagation of explosive sound in shallow water," in Memoir – Geological Society of America (Geological Society of America, Boulder, CO), available at https://pubs.geoscienceworld.org/georef/record/6/4290833/Theory-of-propagation-of-explosive-sound-in.

Pierce, A. D. (**1965**). "Extension of the method of normal modes to sound propagation in an almost-stratified medium," J. Acoust. Soc. Am. **37**(1), 19–27.

Robinson, A. R., and Lermusiaux, P. F. J. (**2004**). "Prediction systems with data assimilation for coupled ocean science and ocean acoustics," in *Proceedings of the Sixth International Conference on Theoretical and Computational Acoustics*, Honolulu, HI, edited by A. Tolstoy (World Scientific Publishing, Singapore), pp. 325–342.

Sapsis, T. P., and Lermusiaux, P. F. J. (**2009**). "Dynamically orthogonal field equations for continuous stochastic dynamical systems," Phys. D: Nonlinear Phenom. **238**(23–24), 2347–2360.

Šimša, J. (**1992**). "The best l2-approximation by finite sums of functions with separable variables," Aeq. Math. **43**(2-3), 248–263.

Strang, G. (**1968**). "On the construction and comparison of difference schemes," SIAM J. Numer. Anal. **5**(3), 506–517.

Tappert, F. D. (**1977**). "The parabolic approximation method," in *Wave Propagation and Underwater Acoustics*, edited by J. B. Keller and J. S. Papadakis (Springer-Verlag, Berlin), pp. 224–287.

Trefethen, L. N., and Bau, D., III. (**1997**). *Numerical Linear Algebra* (SIAM, Philadelphia).

Twomey, E. R., and Signell, R. P. (**2013**). "Construction of a 3-arcsecond digital elevation model for the Gulf of Maine," Open-File Report 2011-1127, U.S. Geological Survey, Reston, VA.

Ueckermann, M. P. (**2014**). "High order hybrid discontinuous Galerkin regional ocean modeling," Ph.D. Thesis, Massachusetts Institute of Technology, Cambridge, MA.

Ueckermann, M. P., and Lermusiaux, P. F. J. (**2016**). "Hybridizable discontinuous Galerkin projection methods for Navier–Stokes and Boussinesq equations," J. Comput. Phys. **306**, 390–421.

Ueckermann, M. P., Lermusiaux, P. F. J., and Sapsis, T. P. (**2013**). "Numerical schemes for dynamically orthogonal equations of stochastic fluid and ocean flows," J. Comput. Phys. **233**, 272–294.

Williams, A. (**1970**). "Normal-mode methods in propagation of underwater sound," in *Underwater Acoustics*, edited by R. W. B. Stephens (Wiley-Interscience, London), pp. 23–56.

Xu, C., and Tang, J. (**2019**). "A propagation matrix method for the solution of the parabolic equation in ocean acoustics," J. Acoust. Soc. Am. **146**(6), EL464–EL469.